Zhang, B., Bao, X., and Xu, Y., 2022, Seismic anisotropy in the central Tien Shan unveils rheology-controlled deformation during intracontinental orogenesis: Geology, v. 50, https://doi.org/10.1130/G49633.1

Seismic anisotropy in the central Tien Shan unveils rheology-controlled deformation during intracontinental orogenesis

Bingfeng Zhang, Xuewei Bao*, and Yixian Xu

Key Laboratory of Geoscience Big Data and Deep Resource of Zhejiang Province, School of Earth Sciences, Zhejiang University, Hangzhou 310027, China

*E-mail: xwbao@zju.edu.cn

Introduction

This document contains detailed descriptions of the data, methods and quality assessment specifics used to obtain seismic anisotropy measurements presented in the paper, discussion on the azimuthal variations of the XKS splitting measurements, as well as Supplementary Figures S1-7 and Tables S1-6. This material is associated with Zhang et al., ***Seismic anisotropy in the central Tien Shan unveils rheology-controlled deformation during intracontinental orogenesis.***

Data

Dataset analyzed in this study mainly comprises broadband seismic waveforms recorded by the Middle AsiaN Active Source (MANAS) project (Makarov et al., 2010). The 40 broadband seismograph stations were deployed along an NNW-SSE profile across the central Tien Shan with an interstation spacing of ~10 km and were operational from July 2005 to July 2007. To better constrain the lateral variation of crustal anisotropic properties, the MANAS data are supplemented with seismograms from several KNET, KRNET, and GHENGIS stations within the distance of 60 km from the profile. All stations, their network affiliations, instruments, and data ranges for data used are listed in Table S3.

Pms moveout fitting

We investigate crustal anisotropy based on the azimuthal variations of Moho Ps conversions on radial RFs. To ensure high quality and sufficient back azimuthal coverage of the analyzed records, we select teleseismic events with epicentral distances between 30° and 95°, a lower cut-off magnitude of 5.5, which is reduced to 4.5 if back azimuth (BAZ) is within the range of 0°-30° and 150°-360°, and good signal-to-noise ratio (SNR). All events are filtered in the frequency band of 0.02-1 Hz and projected into the RTZ coordinates. P wave receiver functions are then calculated using the water-level deconvolution technique (Ammon, 1991), in which water-level is set to 0.01 for enhancing the stability of deconvolution. A gaussian low-pass filter with a Gaussian parameter of 1.5 is also employed to suppress high-frequency noise. We visually inspect all the radial RFs and remove the anomalous ones with no clear Pms phases from further analysis. The number of the retained RFs at individual stations range from 27 to 438, with an average of 145. The corresponding 1697 teleseismic events provide an overall good coverage in both distance and azimuth of the analyzed data (Fig. S3). Then, ‘four-pin’ moveout correction scheme (Chen and Niu, 2013) is implemented to eliminate Pms moveout associated with epicentral distance variations. This correction is made with respect to a ray parameter of 0.06 s/km. RFs within the same azimuthal bin of 10° are also averaged to enhance SNR and to mitigate the effect of RF clusters in some directions.

For a shear wave passing through the anisotropic medium, different degree of splitting occurs depending on the relation between BAZ and fast symmetry axis of the anisotropic medium, leading to the variation in the amplitude and arrival time of the recorded phase with respect to BAZ. Under the assumption of a single-layer anisotropic crust with a horizontal symmetry axis and a flat Moho, the Pms phase on the radial RFs exhibits a four-lobed variation as a function of BAZ (Liu and Niu, 2012), which can be fitted by a $\cos 2\theta$ function. This distinctive characteristic has been widely used to quantify crustal anisotropy, as indicated by fast orientation (φ_{Pms}) and delay time (δt_{Pms}). Note also that systematic Pms moveout can be induced by a tilted Moho, which exhibits a $\cos\theta$ variation in both arrival time and amplitude. In order to robustly estimate crustal anisotropy in the Tien Shan, where both intense crustal deformation and gently dipping Moho are indicated (Zhang et al., 2020), we adopt a least square fitting procedure to fit Pms arrival times on the radial RFs using (1) a $\cos 2\theta$ function and (2) the combination of $\cos\theta$ and $\cos 2\theta$ functions:

$$t_{Pms} = t_{iso} - \frac{\delta t_{Pms}}{2}\cos[2(\theta - \varphi_{Pms})] \qquad (1)$$

$$t_{Pms} = t_{iso} + \frac{A_1}{2}\cos(\theta - \varphi_1) - \frac{\delta t_{Pms}}{2}\cos[2(\theta - \varphi_{Pms})] \qquad (2)$$

where t_{iso} is the arrival time in the isotropic medium, δt_{Pms} reflects the magnitude of crustal anisotropy and is equivalent to the maximum splitting time between fast and slow shear waves, φ_{Pms} represents the fast orientation measured clockwise from the north, A_1 and φ_1 are amplitude and phase terms of the two-lobed variation, θ is the BAZ of the incoming wave. The optimal pair of parameters are obtained in the grid-search for t_{iso}, φ_{Pms}, δt_{Pms} (as well as two-lobed terms A_1 and φ_1 for Equation (2)). The searching range for t_{iso} covers all Pms phases on the back azimuthal profile with an increment of 0.01 s, and those for the other four parameters are listed as follows: φ_{Pms} (0-180° with a step of 2°), φ_1 (0-360° with a step of 2°), δt_{Pms} and A_1 (0-1.5 s with a step of 0.05 s). Standard deviations are estimated using the bootstrapping resampling technique (Efron and Tibshirani, 1986).

Systematic tests on synthetic RFs constructed using the ray summation algorithm (Frederiksen and Bostock, 2000) confirm that both of the harmonic fitting schemes can successfully recover the input anisotropy for an anisotropic crust with a low-angle dipping Moho (see Synthetic Tests for more details). In comparison, the fitting based on Equation (2) gives more robust results, especially for a weakly anisotropic crust, which is presented as the final results. Robust crustal anisotropy measurements in the presence of a tilted Moho are further ensured by quality control based on the following criteria: (1) good BAZ coverage, which is defined as more than 12 azimuthal bins with data and maximum azimuthal gap less than 180°; (2) stations with the δt_{Pms} or A_1 estimation reaching the maximum search range are considered to be unreliable and are not used; (3) coherence between the results given by the two harmonic fitting schemes, with the difference in φ_{Pms} and δt_{Pms} less equal than 25° and 0.3 s, respectively; (4) the uncertainties of the resulting crustal anisotropy as defined in Kong et al. (2016) less equal than 0.4. See Fig. S4 for demonstration of Pms moveout fitting analyses at 42 stations with sufficient BAZ coverage.

XKS splitting

SKS and SKKS waveforms recorded at MANAS stations are processed to delineate the detailed lateral variations of apparent anisotropy in the crust and upper mantle of the Tien Shan. Earthquakes with a cut-off magnitude of 5.6 (which is reduced to 5.5 for events deeper than 100 km) are selected (Fig. S3). The epicentral distance ranges for SKS and SKKS phases are 85-180° and 90-180°, respectively. The seismograms are then band-pass filtered to the main frequency band of the two phases between 4 and 25 s for optimizing their clarity. Those with a low SNR (as defined in Liu and Gao (2013)) or the interference of other major phases in the signal window are not used in the following analysis to improve the reliability of the splitting measurements.

XKS splitting is performed using SplitRacer software (Reiss and Rümpker, 2017), in which the minimization of transverse energy method (Silver and Chan, 1991) is utilized to constrain the SWS parameters, fast orientation (φ_{XKS}) and delay time (δt_{XKS}). XKS window is manually adjusted to further exclude the remaining non-XKS signals. We repeat the processing routine for 50 slightly shifted XKS windows, which allows for the statistical evaluation of the results. Uncertainties are indicated by the 95% confidence region of φ_{XKS} and δt_{XKS} estimated using the inverse F-test (Silver and Chan, 1991), in which the degrees of freedom are overestimated and thus altered in this study based on the findings of Walsh et al. (2013). Individual SWS parameters are derived from the minimum of the 95% confidence region, and then used to construct corrected seismograms that theoretically remove the XKS energy on the transverse component.

Quality of the XKS measurements is evaluated based on the following criteria and classified into four categories (“good”, “fair”, “null” and “poor”): (1) the clarity of XKS phases on the radial and transverse components; (2) the energy reduction on the corrected transverse component; (3) the particle motion before and after correction; (4) the consistency of splitting measurements for different XKS windows; (5) the 95%

confidence level of the measurements; and (6) the proportional characteristic between $\frac{dR}{dt}$ and dT waveforms, which can be utilized to distinguish whether the energy on the transverse component is induced by anisotropy or other structural factors such as small-scale scattering. "poor" measurements are not used for interpretation. An example of "good" measurement at station XP-DAMB for the event 2006-03-07-06:28:55 is presented in Fig. S5.

Synthetic Tests

We present additional tests that we performed on synthetic datasets, which demonstrate the robustness of crustal anisotropy measurements in the presence of a titled Moho.

We design a series of crustal models with Moho dip and anisotropy of different magnitudes and geometries (Table S4). Synthetic seismograms are constructed based on the ray summation algorithm and then transformed into RFs. To test the reliability of the measurements when dealing with real-world data, we synthesized RFs and add random Gaussian noise using the event distributions of three representative MANAS stations (Table S5). We test a total of 21 cases, which are listed in Table S6. An example of harmonic fitting results for Case 13 is presented in Fig. S6.

Cases 02 and 03 show expected anisotropy measurements under ideal conditions for two end-member models: dipping Moho and azimuthal anisotropy, respectively. The stability of the method is evaluated by its capability to recover the input anisotropy in more practical cases of dipping Moho, uneven back azimuthal distribution, and noisy data. In all test cases, the measured crustal anisotropy is consistent with expectations, and the small deviations are within the acceptable range. This indicates that the proposed method is applicable to anisotropy studies in the central Tien Shan, where a gently dipping Moho is imaged and the recorded teleseismic events are mostly clustered in the western Pacific and the Java trench (Fig. S3).

The two harmonic fitting schemes give similar results in most cases, which can be used to identify and reject unstable measurements. As the sole exception, the measured fast orientations with $\cos 2\theta$ harmonic deviates from the model setup by up to 28 degrees when the crust is weakly anisotropic and the back azimuthal coverage is limited (e.g., Case 06). Therefore, harmonic fitting with $\cos\theta$ and $\cos 2\theta$ harmonics are considered more robust.

Azimuthal Variations of XKS Splitting Measurements

Station-averaged XKS splitting measurements are only meaningful under the assumption of simple anisotropy, which is characterized by a single layer of azimuthal anisotropy with a horizontal symmetry axis or a pile of horizontal layers with parallel or orthogonal symmetry axes (Liu and Gao, 2013). This assumption is valid for the case in the central Tien Shan, where our shear wave splitting analyses reveal the sub-orthogonal and sub-parallel fast orientations between the crust and upper mantle of the NCTS and SCTS, respectively. For such simple anisotropy, splitting parameters should be independent of the polarization direction of the incoming wave. It's therefore puzzling to find the explicit azimuthal variations of individual splitting measurements obtained in this study (Fig. S2). Note that similar azimuthal patterns are also reported by Cherie et al. (2016) based on XKS splitting measurements obtained at 25 stations in the central Tien Shan, which the authors propose to be associated with the two-layer anisotropy beneath the mountains (lower layer: -65°, 1.7 s; upper layer: 77°, 1.4 s).

Here we also grid-search for the best-fit two-layer anisotropy parameters for all stations, NCTS stations and SCTS stations, respectively. The misfit function and weighting factors are set to be the same as in Cherie et al. (2016). The searching range for fast orientations is 0° to 180° with an increment of 10°, and that for the delay times is 0–2.4 s with a step of 0.2 s. All possible two-layer anisotropy models that exhibit misfits within 105% of the minimum value along with the predicted azimuthal variations are presented in Fig. S2. The results suffer from serious non-uniqueness problems due to trade-offs among the four parameters as well as the inadequate azimuthal coverage, leading to considerable ambiguity of azimuthal variations in the BAZ range of 50-75° (in modulo-90° domain). Despite the unsuccessful attempt to acquire two-layer parameters, we notice that none of the measured fast orientations are parallel or orthogonal to the BAZ, inconsistent with the two-layer anisotropy assumption.

One of the limitations of the shear wave splitting technique is the lack of depth resolution. The splitting of the XKS phases can be attributed to anisotropic mediums at arbitrary depth from the core-mantle boundary to the surface along the ray path. While much of the lower mantle is thought to be nearly isotropic, there are robust observations of strong anisotropy along the edges of African and Pacific LLSVPs (Deng et al., 2017; Lynner and Long, 2014), as well as the mesoscale Perm Anomaly (Long and Lynner, 2015). In both this study and Cherie et al. (2016), the BAZs of the incoming waves are restricted to three groups (Fig. S3): 80-110°, 270-330°, and 350-360° (hereafter referred to as Group A, B, and C, respectively). In contrast to the measurements of the Group A, in which the fast orientations generally fluctuate around the regional average of 64°, the fast orientations are systematically higher (>64°) and lower (<64°) for Groups B and C, respectively (Fig. S2). When all measurements are projected to their piercing points at 2700 km depth (Fig. S7), we notice that Group B and C measurements are located near the edge of the Perm Anomaly as delineated by cluster analysis. This geographic pattern hints that the azimuthal variations of the XKS measurements may be associated with the localized deformation in the lowermost mantle.

References for Data Repository

Ammon, C. J., 1991, The isolation of receiver effects from teleseismic P waveforms: Bulletin of the Seismological Society of America, v. 81, no. 6, p. 2504-2510.

Chen, Y., and Niu, F., 2013, Ray-parameter based stacking and enhanced pre-conditioning for stable inversion of receiver function data: Geophysical Journal International, v. 194, no. 3, p. 1682-1700.

Cherie, S. G., Gao, S. S., Liu, K. H., Elsheikh, A. A., Kong, F., Reed, C. A., and Yang, B. B., 2016, Shear wave splitting analyses in Tian Shan: Geodynamic implications of complex seismic anisotropy: Geochemistry, Geophysics, Geosystems, v. 17, no. 6, p. 1975-1989.

Deng, J., Long, M. D., Creasy, N., Wagner, L., Beck, S., Zandt, G., Tavera, H., and Minaya, E., 2017, Lowermost mantle anisotropy near the eastern edge of the Pacific LLSVP: Constraints from SKS–SKKS splitting intensity measurements: Geophysical Journal International, v. 210, no. 2, p. 774-786.

Efron, B., and Tibshirani, R., 1986, Bootstrap methods for standard errors, confidence intervals, and other measures of statistical accuracy: Statistical Science, v. 1, no. 1, p. 54-77.

Frederiksen, A. W., and Bostock, M. G., 2000, Modelling teleseismic waves in dipping anisotropic structures: Geophysical Journal International, v. 141, no. 2, p. 401-412.

Kong, F., Wu, J., Liu, K. H., and Gao, S. S., 2016, Crustal anisotropy and ductile flow beneath the eastern Tibetan Plateau and adjacent areas: Earth and Planetary Science Letters, v. 442, p. 72-79.

Lekic, V., Cottaar, S., Dziewonski, A., and Romanowicz, B., 2012, Cluster analysis of global lower mantle tomography: A new class of structure and implications for chemical heterogeneity: Earth and Planetary Science Letters, v. 357-358, p. 68-77.

Liu, H., and Niu, F., 2012, Estimating crustal seismic anisotropy with a joint analysis of radial and transverse receiver function data: Geophysical Journal International, v. 188, no. 1, p. 144-164.

Liu, K. H., and Gao, S. S., 2013, Making reliable shear‐wave splitting measurements: Bulletin of the Seismological Society of America, v. 103, no. 5, p. 2680-2693.

Long, M. D., and Lynner, C., 2015, Seismic anisotropy in the lowermost mantle near the Perm Anomaly: Geophysical Research Letters, v. 42, no. 17, p. 7073-7080.

Lynner, C., and Long, M. D., 2014, Lowermost mantle anisotropy and deformation along the boundary of the African LLSVP: Geophysical Research Letters, v. 41, no. 10, p. 3447-3454.

Makarov, V. I., Alekseev, D. V., Batalev, V. Y., Bataleva, E. A., Belyaev, I. V., Bragin, V. D., Dergunov, N. T., Efimova, N. N., Leonov, M. G., Munirova, L. M., Pavlenkin, A. D., Roecker, S., Roslov, Y. V., Rybin, A. K., and Shchelochkov,

G. G., 2010, Underthrusting of Tarim beneath the Tien Shan and deep structure of their junction zone: Main results of seismic experiment along MANAS Profile Kashgar-Song-Köl: Geotectonics, v. 44, no. 2, p. 102-126.

Reiss, M. C., and Rümpker, G., 2017, SplitRacer: MATLAB code and GUI for semiautomated analysis and interpretation of teleseismic shear‐wave splitting: Seismological Research Letters, v. 88, no. 2A, p. 392-409.

Silver, P. G., and Chan, W. W., 1991, Shear wave splitting and subcontinental mantle deformation: Journal of Geophysical Research, v. 96, no. B10, p. 16429-16454.

Walsh, E., Arnold, R., and Savage, M. K., 2013, Silver and Chan revisited: Journal of Geophysical Research: Solid Earth, v. 118, no. 10, p. 5500-5515.

Zhang, B., Bao, X., and Xu, Y., 2020, Distinct orogenic processes in the South‐ and North‐Central Tien Shan from receiver functions: Geophysical Research Letters, v. 47, no. 6, p. e2019GL086941.

Supplementary Figures and Tables

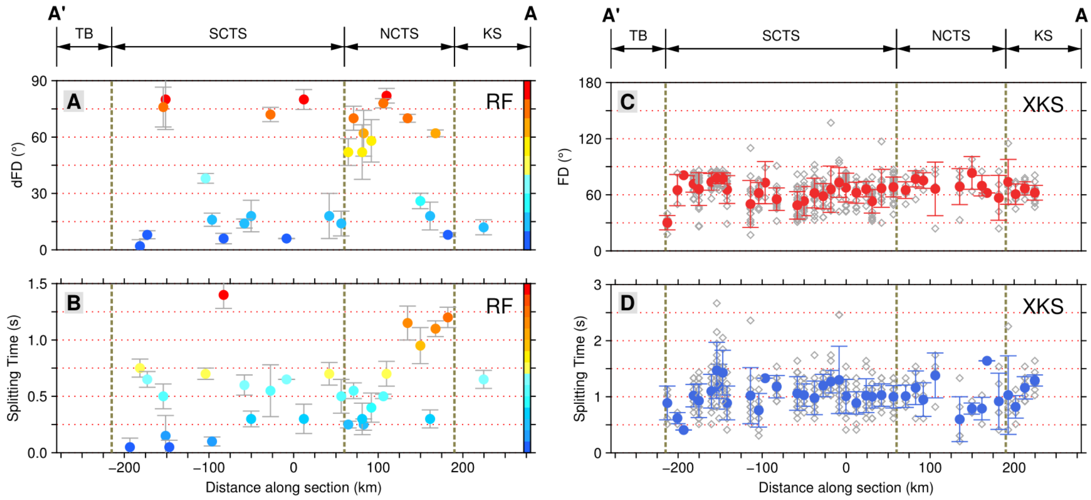

Figure S1. (A-B) Pms moveout fitting parameters plotted along profile A-A′. Fast orientations are shown as dFD, the differential angle with the strike of the mountains (~70°). Uncertainties are marked by gray bars. Major tectonic segments are also labeled. (C-D) XKS splitting parameters plotted along profile A-A′. The layout is similar to that of (A-B), but with fast orientations shown as the original values. The individual and station-averaged XKS splitting measurements are indicated by the open diamonds and filled circles, respectively.

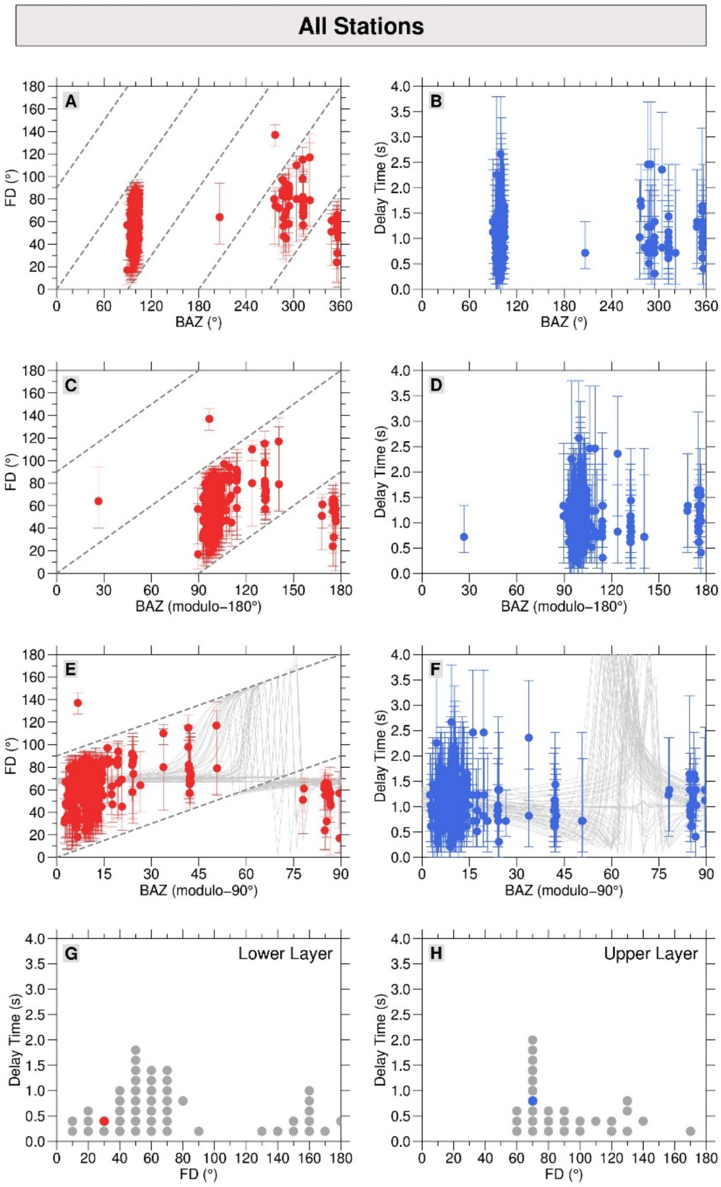

Figure S2. Azimuthal variations of XKS splitting parameters for all, NCTS, and SCTS stations, respectively. (A-B) Fast orientations and delay time plotted against BAZ. The gray dashed lines in (A) show $FD = n \times 90 + BAZ\ (n = -3, -2, -1,\ 0\ and\ 1)$, along which the fast orientation is parallel or orthogonal to the BAZ. Theoretically, there should be no measurements plotted along these lines for simple anisotropy, which is exactly the case for the central Tien Shan. (C-D) Same as (A-B) but for modulo-180° BAZ. (E-F) Same as (A-B) but for modulo-90° BAZ. The azimuthal variations of predicted splitting parameters are also plotted for all possible two-layer anisotropy models that exhibit misfits within 105% of the minimum value. (G-H) Best-fit (colored) and all possible (gray) two-layer anisotropy parameters for the lower and upper layers, respectively. (To be continued)

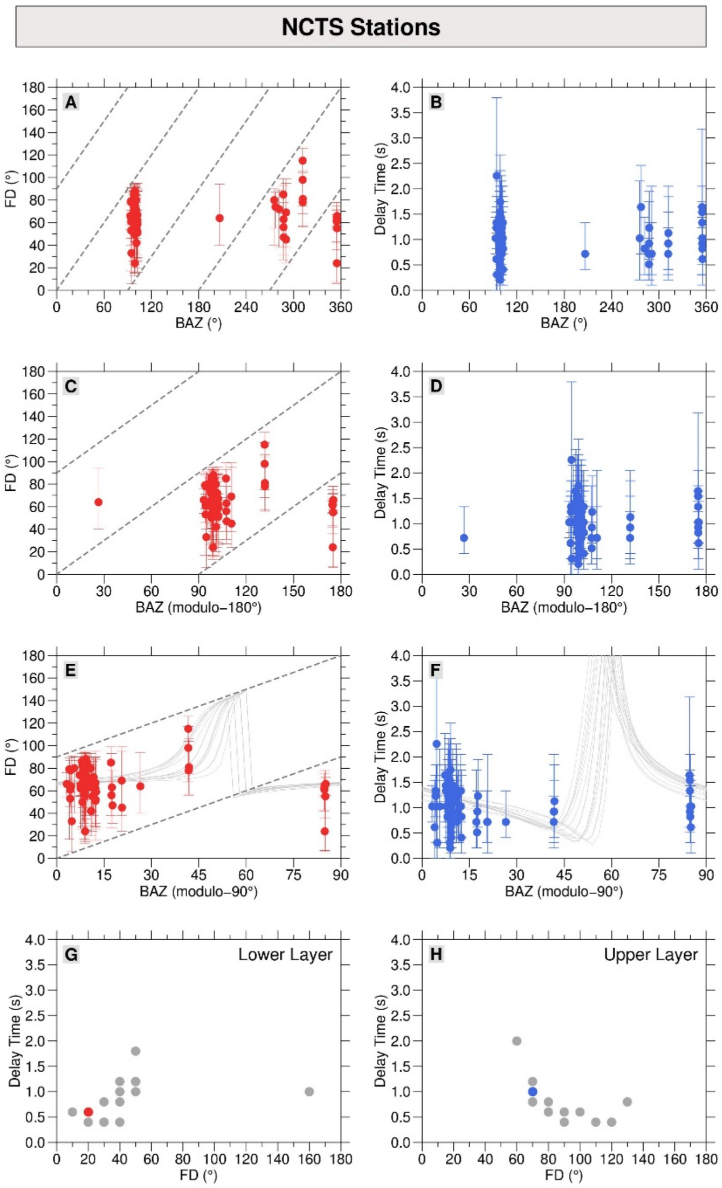

Figure S2. (Continued)

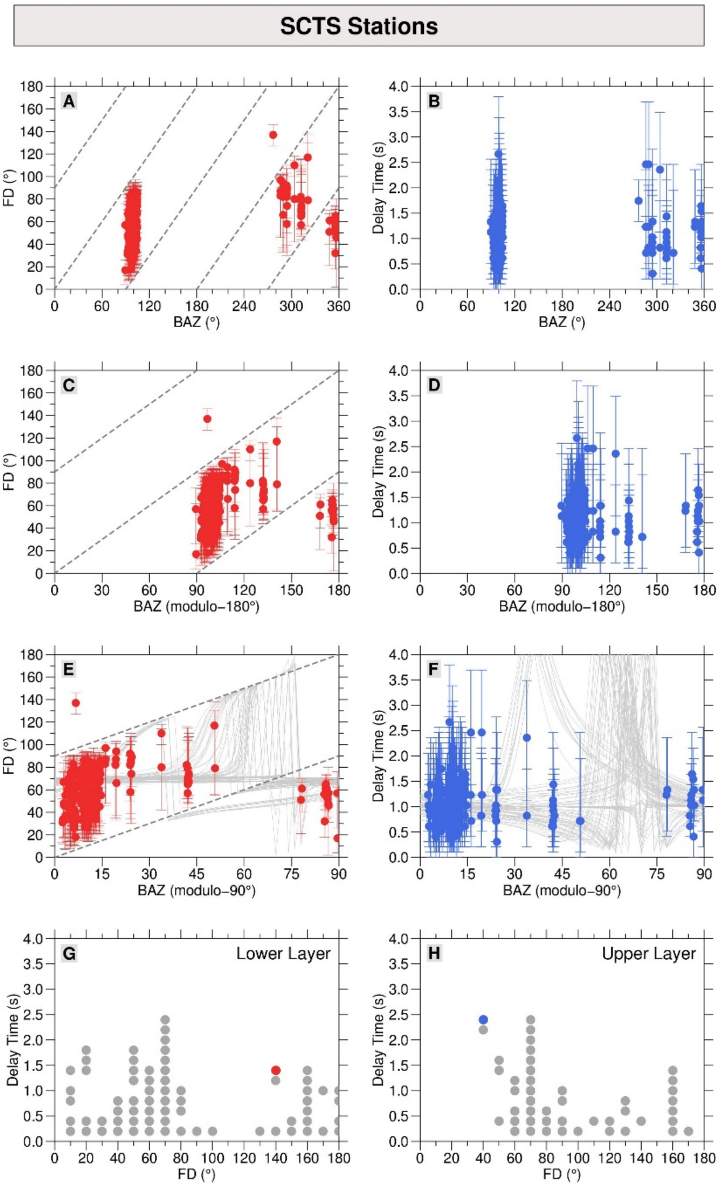

Figure S2. (Continued)

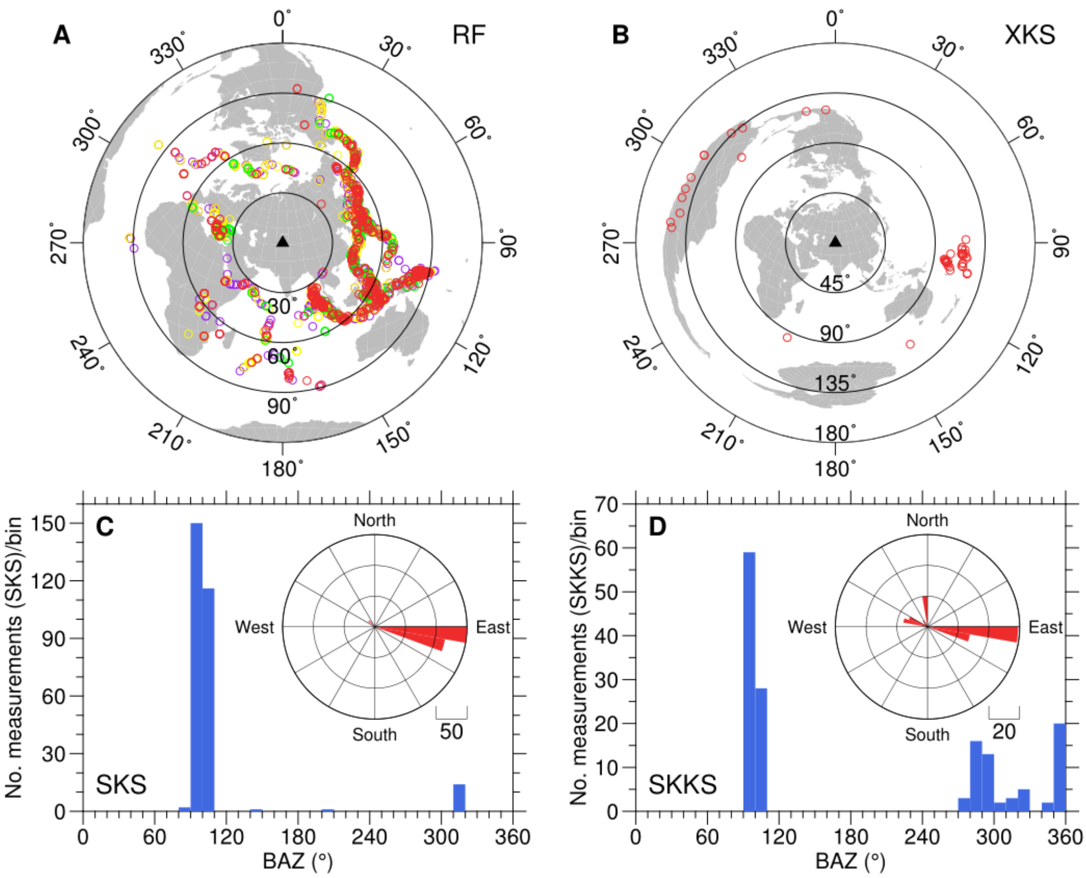

Figure S3. The locations of teleseismic events (A-B) and the back azimuthal distribution of XKS splitting measurements (C-D). Earthquakes recorded by different networks are represented by open circles with different colors (red: MANAS, yellow: KRNET, green: GHENGIS, and purple: KNET).

Good Measurements (27 stations in total)

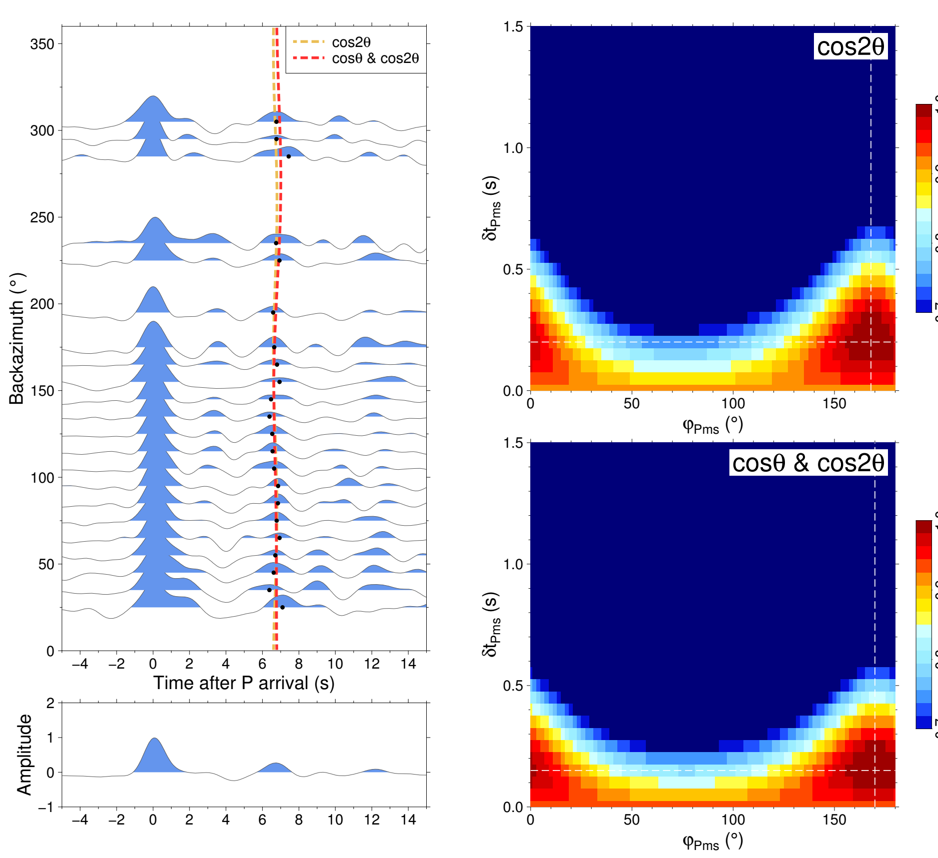

XP–AHQI

cos2θ

t_{iso}: 6.7 s

φ_{Pms}: 168°

δt_{Pms}: 0.20 s

cosθ & cos2θ

t_{iso}: 6.8 s

φ_{Pms}: 170°

δt_{Pms}: 0.15 s

φ_1: 292°

A_1: 0.30 s

uncertainty: 0.36

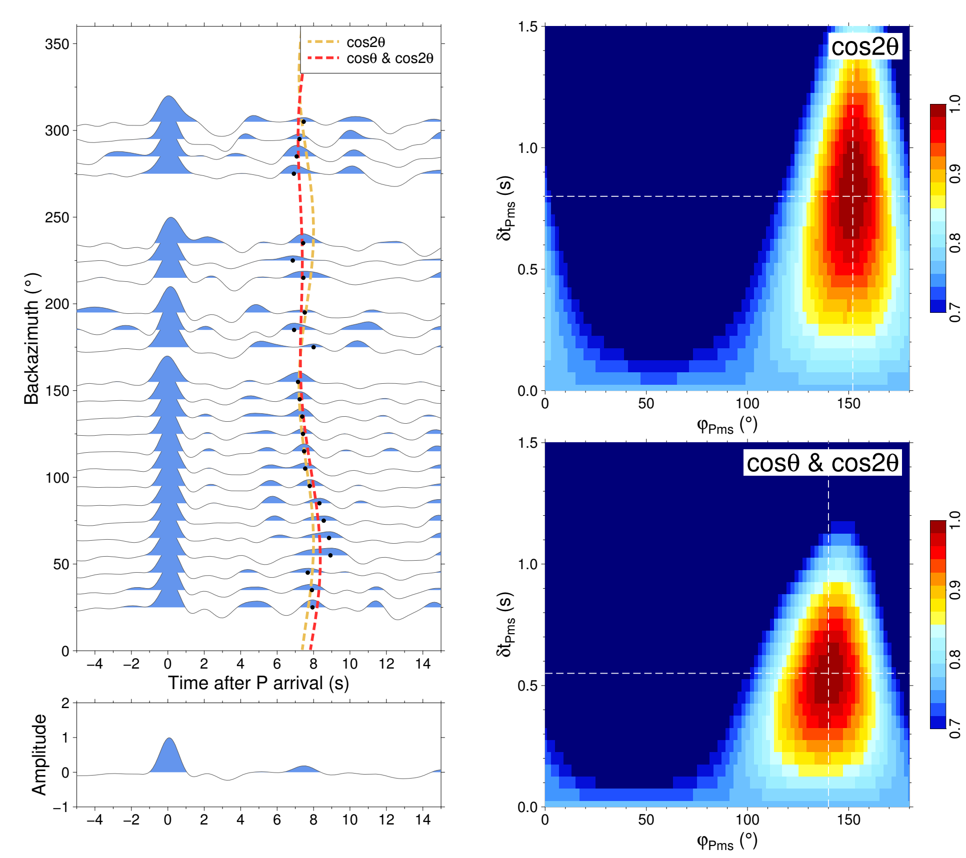

XP–BESM

cos2θ

t_{iso}: 7.6 s

φ_{Pms}: 152°

δt_{Pms}: 0.80 s

cosθ & cos2θ

t_{iso}: 7.6 s

φ_{Pms}: 140°

δt_{Pms}: 0.55 s

φ_1: 58°

A_1: 1.00 s

uncertainty: 0.14

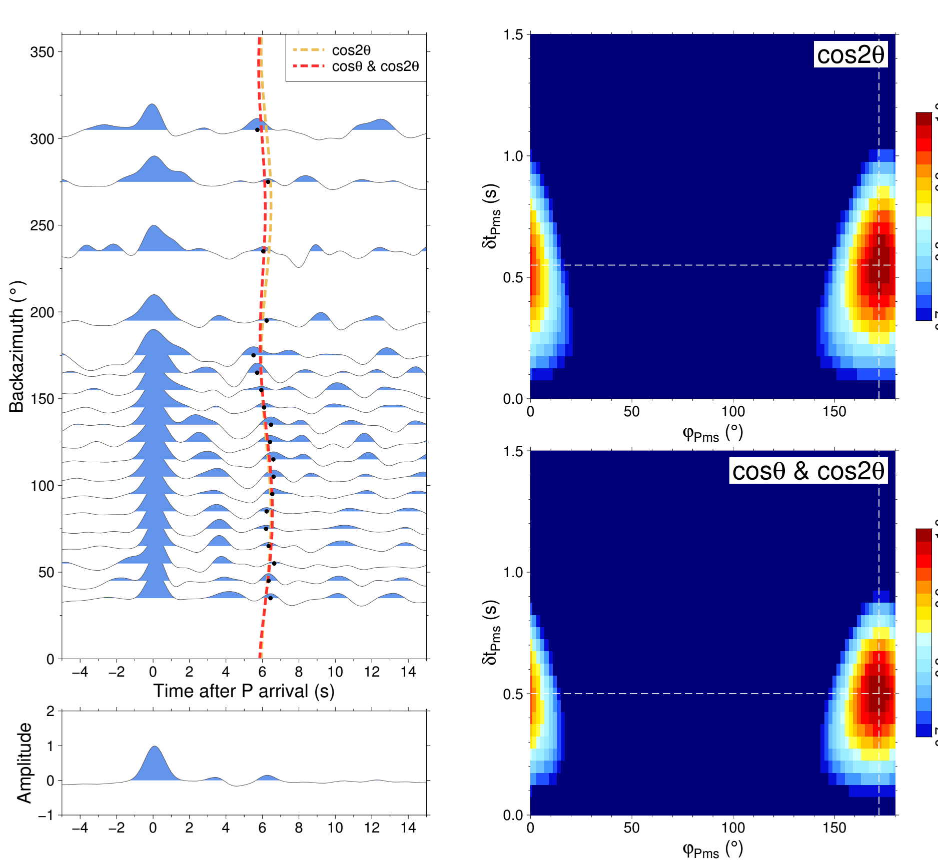

XP–BOOB

cos2θ

t_{iso}: 6.2 s

φ_{Pms}: 172°

δt_{Pms}: 0.55 s

cosθ & cos2θ

t_{iso}: 6.1 s

φ_{Pms}: 172°

δt_{Pms}: 0.50 s

φ_1: 94°

A_1: 0.40 s

uncertainty: 0.05

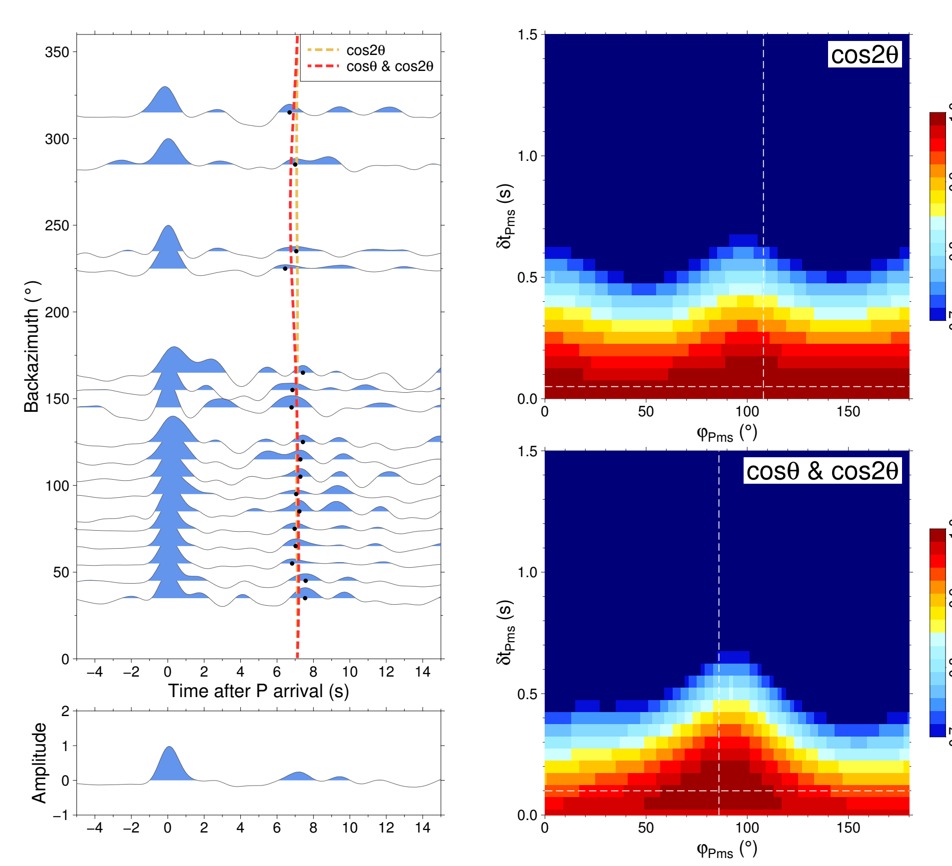

XP–BRID

cos2θ

t_{iso}: 7.1 s

φ_{Pms}: 108°

δt_{Pms}: 0.05 s

cosθ & cos2θ

t_{iso}: 7.0 s

φ_{Pms}: 86°

δt_{Pms}: 0.10 s

φ_1: 72°

A_1: 0.45 s

uncertainty: 0.08

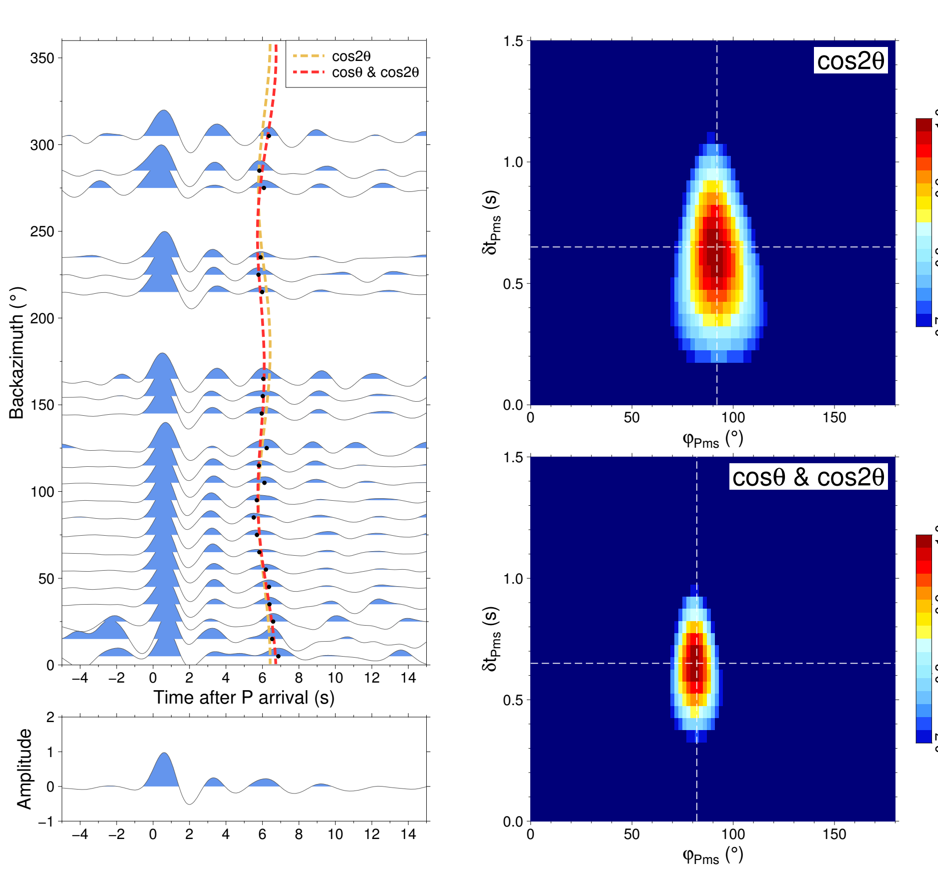

XP–CHIC

cos2θ

t_{iso}: 6.1 s

φ_{Pms}: 92°

δt_{Pms}: 0.65 s

cosθ & cos2θ

t_{iso}: 6.1 s

φ_{Pms}: 82°

δt_{Pms}: 0.65 s

φ_1: 354°

A_1: 0.65 s

uncertainty: 0.12

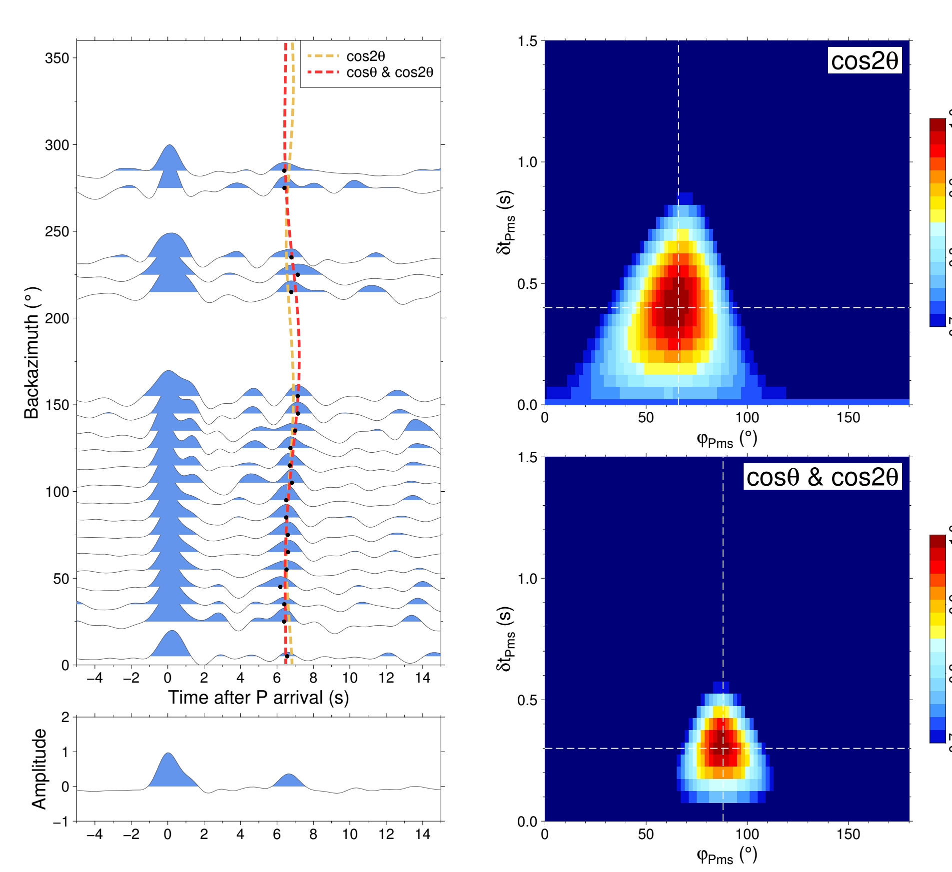

XP–DAMB

cos2θ

t_{iso}: 6.7 s

φ_{Pms}: 66°

δt_{Pms}: 0.40 s

cosθ & cos2θ

t_{iso}: 6.7 s

φ_{Pms}: 88°

δt_{Pms}: 0.30 s

φ_1: 176°

A_1: 0.75 s

uncertainty: 0.16

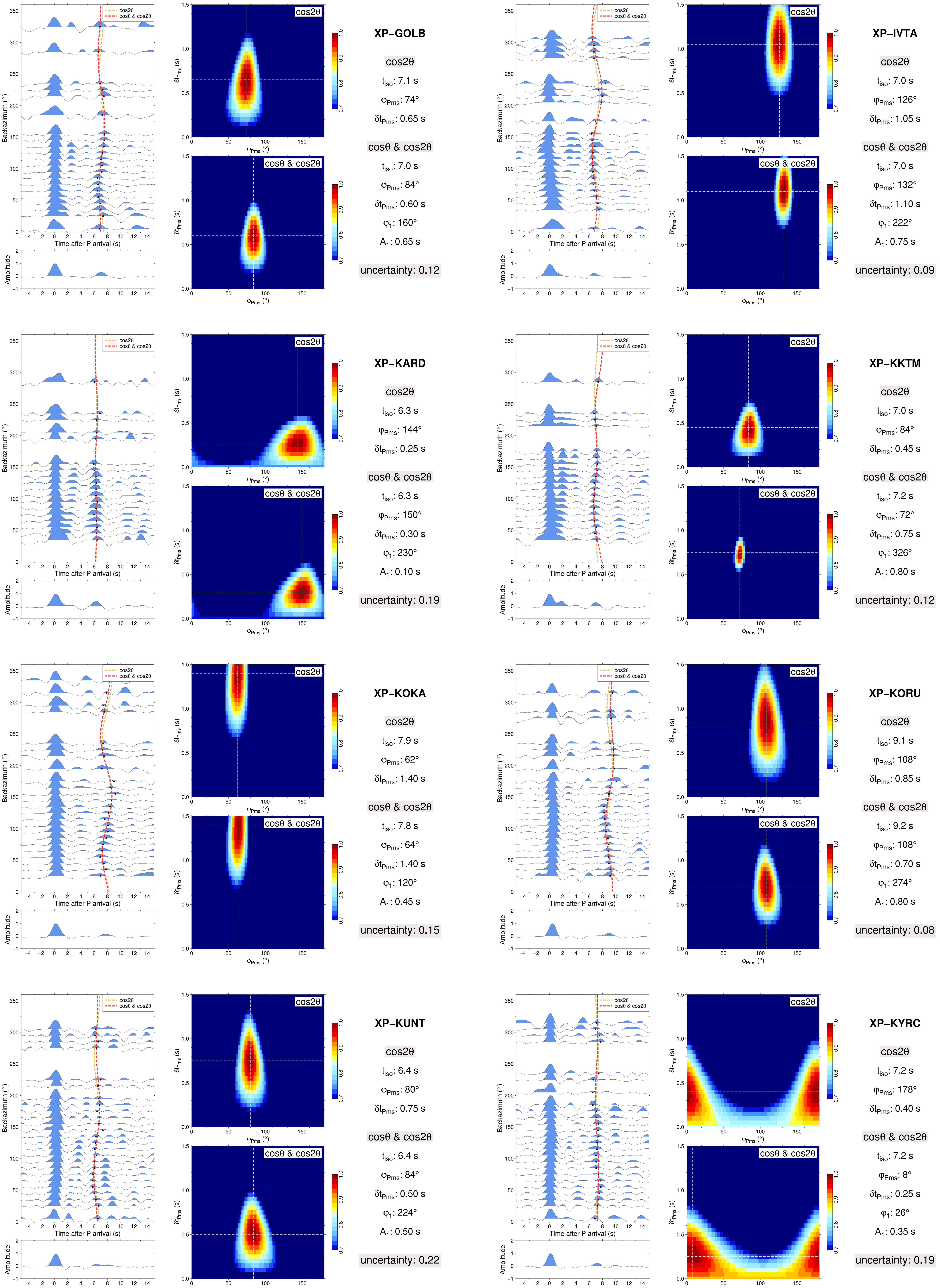
XP−GOLB
cos2θ
t_{iso}: 7.1 s
φ_{Pms}: 74°
δt_{Pms}: 0.65 s
cosθ & cos2θ
t_{iso}: 7.0 s
φ_{Pms}: 84°
δt_{Pms}: 0.60 s
φ_1: 160°
A_1: 0.65 s
uncertainty: 0.12
XP−IVTA
cos2θ
t_{iso}: 7.0 s
φ_{Pms}: 126°
δt_{Pms}: 1.05 s
cosθ & cos2θ
t_{iso}: 7.0 s
φ_{Pms}: 132°
δt_{Pms}: 1.10 s
φ_1: 222°
A_1: 0.75 s
uncertainty: 0.09
XP−KARD
cos2θ
t_{iso}: 6.3 s
φ_{Pms}: 144°
δt_{Pms}: 0.25 s
cosθ & cos2θ
t_{iso}: 6.3 s
φ_{Pms}: 150°
δt_{Pms}: 0.30 s
φ_1: 230°
A_1: 0.10 s
uncertainty: 0.19
XP−KKTM
cos2θ
t_{iso}: 7.0 s
φ_{Pms}: 84°
δt_{Pms}: 0.45 s
cosθ & cos2θ
t_{iso}: 7.2 s
φ_{Pms}: 72°
δt_{Pms}: 0.75 s
φ_1: 326°
A_1: 0.80 s
uncertainty: 0.12
XP−KOKA
cos2θ
t_{iso}: 7.9 s
φ_{Pms}: 62°
δt_{Pms}: 1.40 s
cosθ & cos2θ
t_{iso}: 7.8 s
φ_{Pms}: 64°
δt_{Pms}: 1.40 s
φ_1: 120°
A_1: 0.45 s
uncertainty: 0.15
XP−KORU
cos2θ
t_{iso}: 9.1 s
φ_{Pms}: 108°
δt_{Pms}: 0.85 s
cosθ & cos2θ
t_{iso}: 9.2 s
φ_{Pms}: 108°
δt_{Pms}: 0.70 s
φ_1: 274°
A_1: 0.80 s
uncertainty: 0.08
XP−KUNT
cos2θ
t_{iso}: 6.4 s
φ_{Pms}: 80°
δt_{Pms}: 0.75 s
cosθ & cos2θ
t_{iso}: 6.4 s
φ_{Pms}: 84°
δt_{Pms}: 0.50 s
φ_1: 224°
A_1: 0.50 s
uncertainty: 0.22
XP−KYRC
cos2θ
t_{iso}: 7.2 s
φ_{Pms}: 178°
δt_{Pms}: 0.40 s
cosθ & cos2θ
t_{iso}: 7.2 s
φ_{Pms}: 8°
δt_{Pms}: 0.25 s
φ_1: 26°
A_1: 0.35 s
uncertainty: 0.19
Backazimuth (°)
Time after P arrival (s)
Amplitude
δt_{Pms} (s)
φ_{Pms} (°)
cos2θ
cosθ & cos2θ

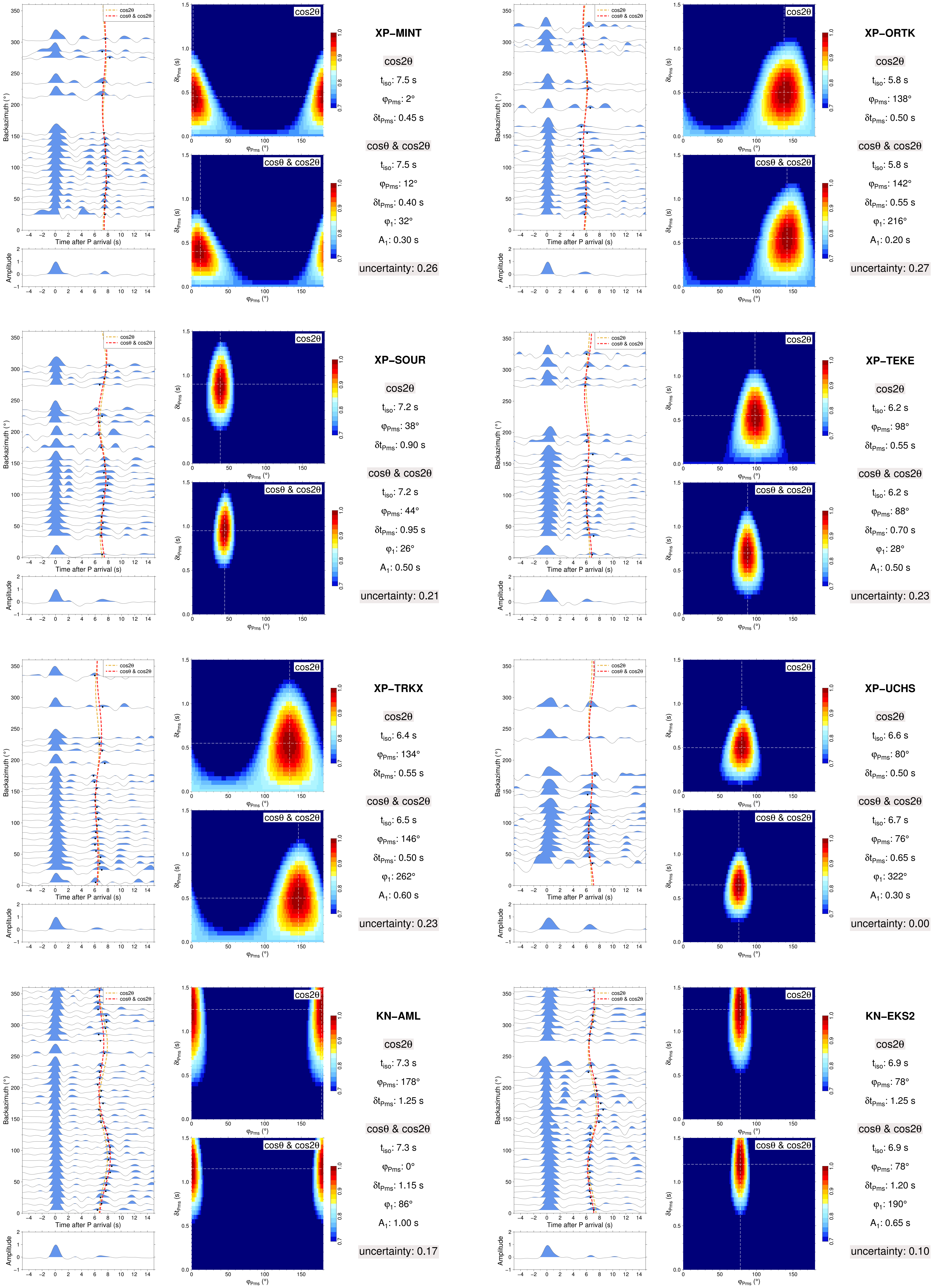
XP−MINT
cos2θ
t_{iso}: 7.5 s
φ_{Pms}: 2°
δt_{Pms}: 0.45 s
cosθ & cos2θ
t_{iso}: 7.5 s
φ_{Pms}: 12°
δt_{Pms}: 0.40 s
φ_1: 32°
A_1: 0.30 s
uncertainty: 0.26
XP−ORTK
cos2θ
t_{iso}: 5.8 s
φ_{Pms}: 138°
δt_{Pms}: 0.50 s
cosθ & cos2θ
t_{iso}: 5.8 s
φ_{Pms}: 142°
δt_{Pms}: 0.55 s
φ_1: 216°
A_1: 0.20 s
uncertainty: 0.27
XP−SOUR
cos2θ
t_{iso}: 7.2 s
φ_{Pms}: 38°
δt_{Pms}: 0.90 s
cosθ & cos2θ
t_{iso}: 7.2 s
φ_{Pms}: 44°
δt_{Pms}: 0.95 s
φ_1: 26°
A_1: 0.50 s
uncertainty: 0.21
XP−TEKE
cos2θ
t_{iso}: 6.2 s
φ_{Pms}: 98°
δt_{Pms}: 0.55 s
cosθ & cos2θ
t_{iso}: 6.2 s
φ_{Pms}: 88°
δt_{Pms}: 0.70 s
φ_1: 28°
A_1: 0.50 s
uncertainty: 0.23
XP−TRKX
cos2θ
t_{iso}: 6.4 s
φ_{Pms}: 134°
δt_{Pms}: 0.55 s
cosθ & cos2θ
t_{iso}: 6.5 s
φ_{Pms}: 146°
δt_{Pms}: 0.50 s
φ_1: 262°
A_1: 0.60 s
uncertainty: 0.23
XP−UCHS
cos2θ
t_{iso}: 6.6 s
φ_{Pms}: 80°
δt_{Pms}: 0.50 s
cosθ & cos2θ
t_{iso}: 6.7 s
φ_{Pms}: 76°
δt_{Pms}: 0.65 s
φ_1: 322°
A_1: 0.30 s
uncertainty: 0.00
KN−AML
cos2θ
t_{iso}: 7.3 s
φ_{Pms}: 178°
δt_{Pms}: 1.25 s
cosθ & cos2θ
t_{iso}: 7.3 s
φ_{Pms}: 0°
δt_{Pms}: 1.15 s
φ_1: 86°
A_1: 1.00 s
uncertainty: 0.17
KN−EKS2
cos2θ
t_{iso}: 6.9 s
φ_{Pms}: 78°
δt_{Pms}: 1.25 s
cosθ & cos2θ
t_{iso}: 6.9 s
φ_{Pms}: 78°
δt_{Pms}: 1.20 s
φ_1: 190°
A_1: 0.65 s
uncertainty: 0.10
Backazimuth (°)
Time after P arrival (s)
Amplitude
δt_{Pms} (s)
φ_{Pms} (°)

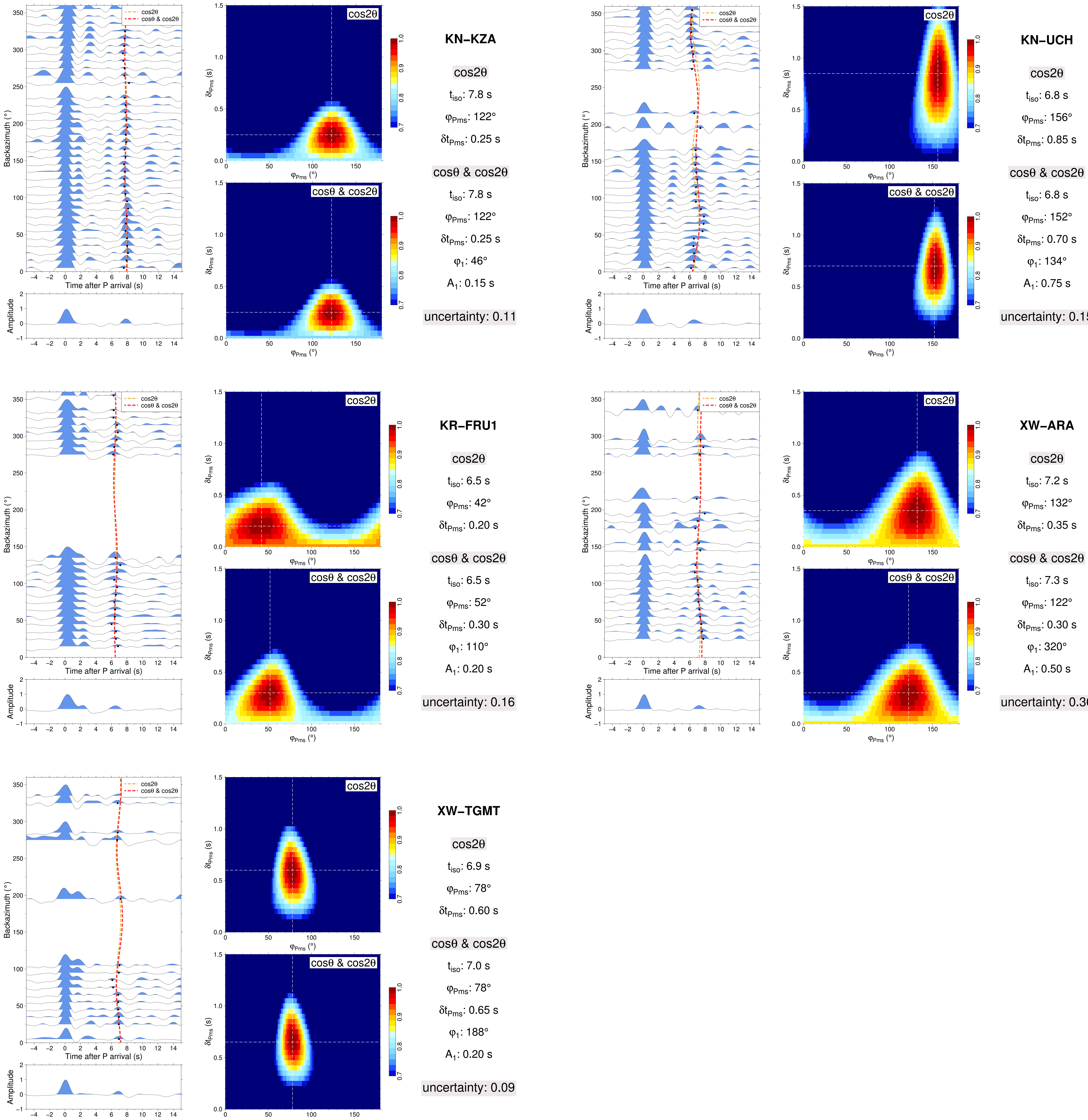

Poor Measurements: d_φ_{Pms} > 25° or d_δt_{Pms} > 0.3 s (11 stations in total)

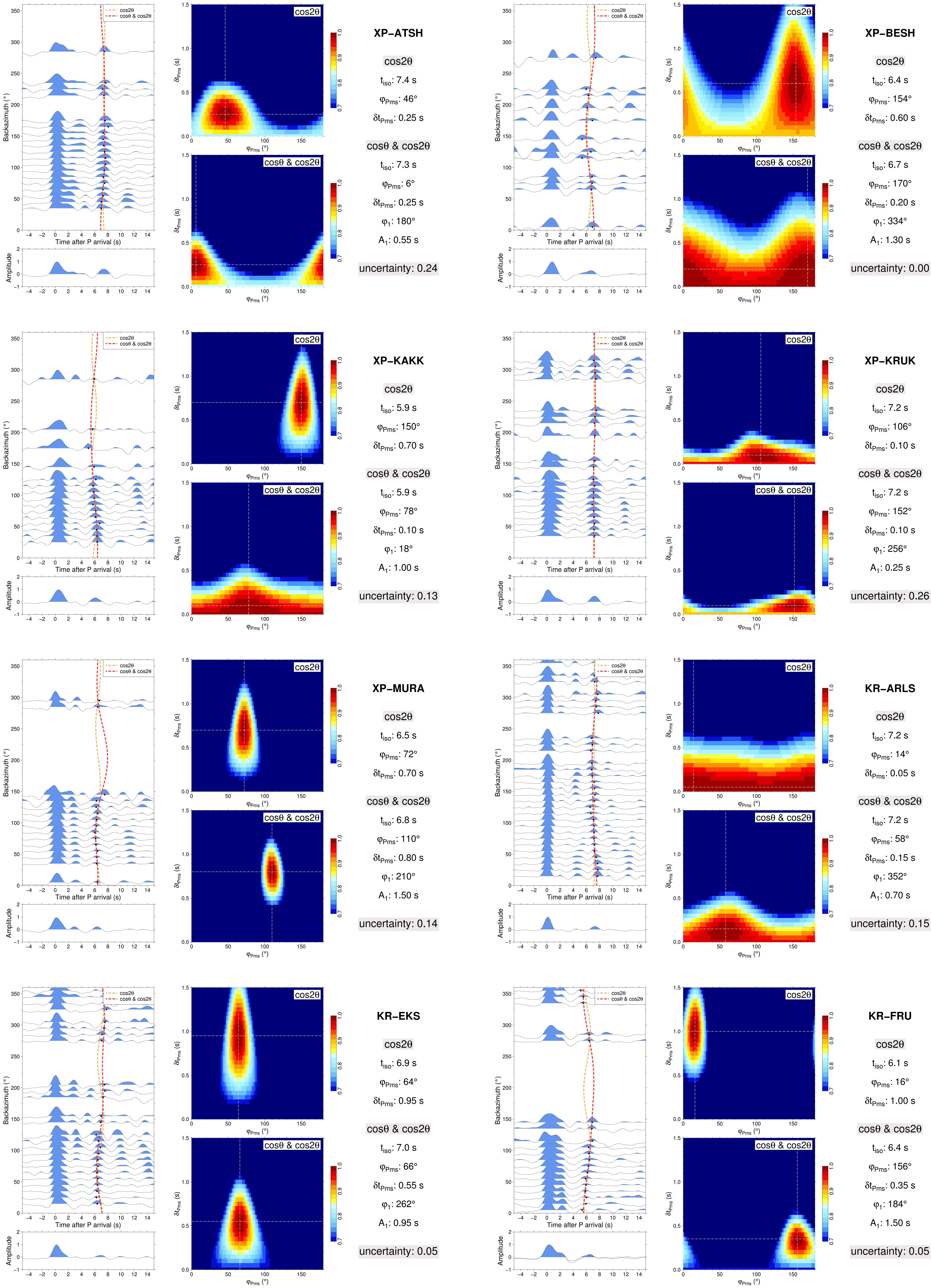
XP–ATSH
cos2θ
t_iso: 7.4 s
φ_Pms: 46°
δt_Pms: 0.25 s
cosθ & cos2θ
t_iso: 7.3 s
φ_Pms: 6°
δt_Pms: 0.25 s
φ_1: 180°
A_1: 0.55 s
uncertainty: 0.24
XP–BESH
cos2θ
t_iso: 6.4 s
φ_Pms: 154°
δt_Pms: 0.60 s
cosθ & cos2θ
t_iso: 6.7 s
φ_Pms: 170°
δt_Pms: 0.20 s
φ_1: 334°
A_1: 1.30 s
uncertainty: 0.00
XP–KAKK
cos2θ
t_iso: 5.9 s
φ_Pms: 150°
δt_Pms: 0.70 s
cosθ & cos2θ
t_iso: 5.9 s
φ_Pms: 78°
δt_Pms: 0.10 s
φ_1: 18°
A_1: 1.00 s
uncertainty: 0.13
XP–KRUK
cos2θ
t_iso: 7.2 s
φ_Pms: 106°
δt_Pms: 0.10 s
cosθ & cos2θ
t_iso: 7.2 s
φ_Pms: 152°
δt_Pms: 0.10 s
φ_1: 256°
A_1: 0.25 s
uncertainty: 0.26
XP–MURA
cos2θ
t_iso: 6.5 s
φ_Pms: 72°
δt_Pms: 0.70 s
cosθ & cos2θ
t_iso: 6.8 s
φ_Pms: 110°
δt_Pms: 0.80 s
φ_1: 210°
A_1: 1.50 s
uncertainty: 0.14
KR–ARLS
cos2θ
t_iso: 7.2 s
φ_Pms: 14°
δt_Pms: 0.05 s
cosθ & cos2θ
t_iso: 7.2 s
φ_Pms: 58°
δt_Pms: 0.15 s
φ_1: 352°
A_1: 0.70 s
uncertainty: 0.15
KR–EKS
cos2θ
t_iso: 6.9 s
φ_Pms: 64°
δt_Pms: 0.95 s
cosθ & cos2θ
t_iso: 7.0 s
φ_Pms: 66°
δt_Pms: 0.55 s
φ_1: 262°
A_1: 0.95 s
uncertainty: 0.05
KR–FRU
cos2θ
t_iso: 6.1 s
φ_Pms: 16°
δt_Pms: 1.00 s
cosθ & cos2θ
t_iso: 6.4 s
φ_Pms: 156°
δt_Pms: 0.35 s
φ_1: 184°
A_1: 1.50 s
uncertainty: 0.05
Backazimuth (°)
Time after P arrival (s)
Amplitude
δt_Pms (s)
φ_Pms (°)

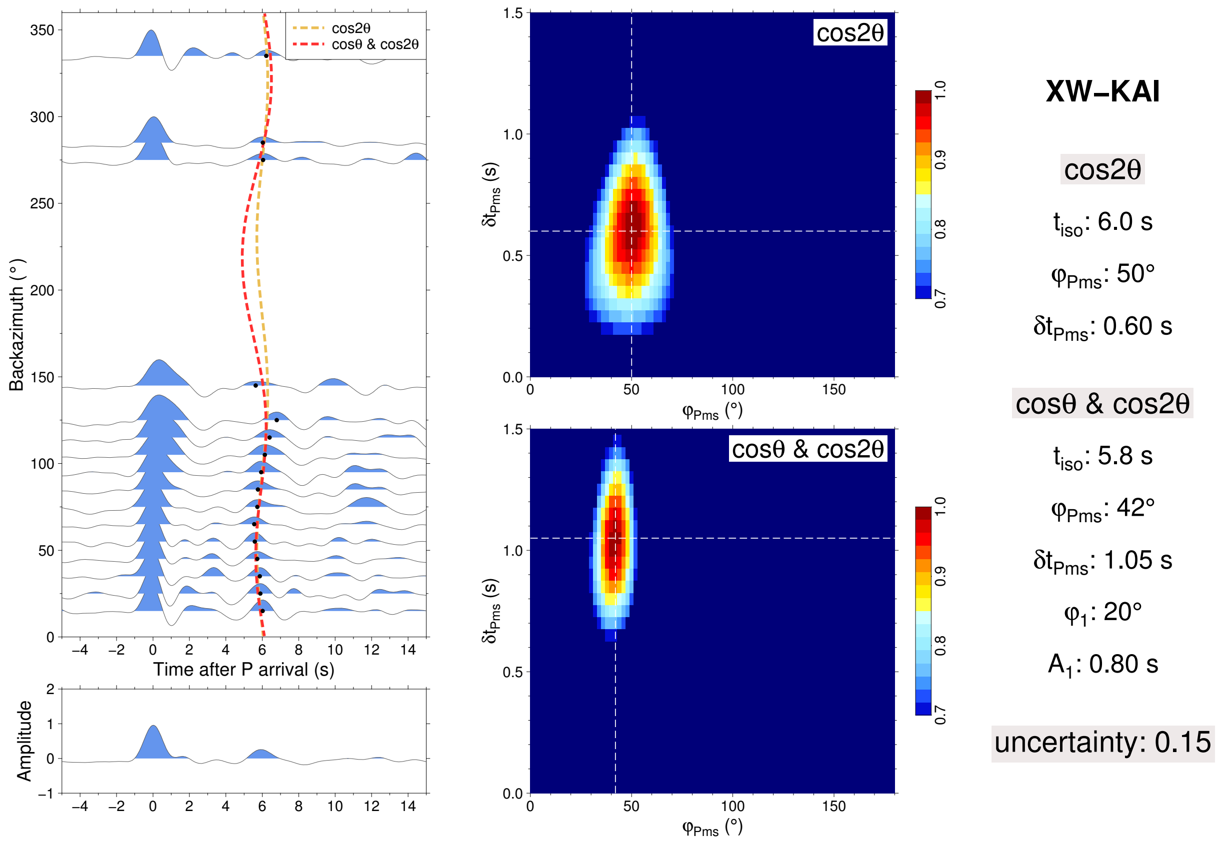

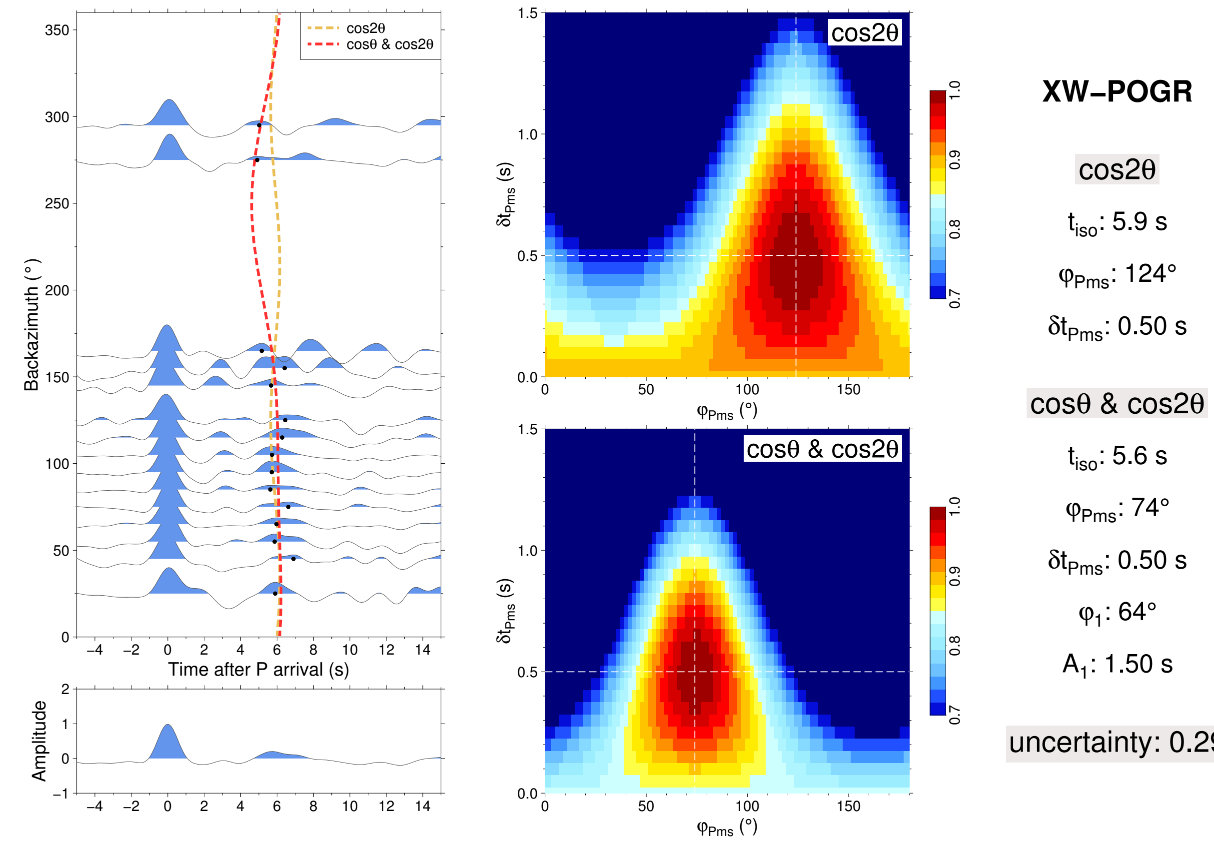

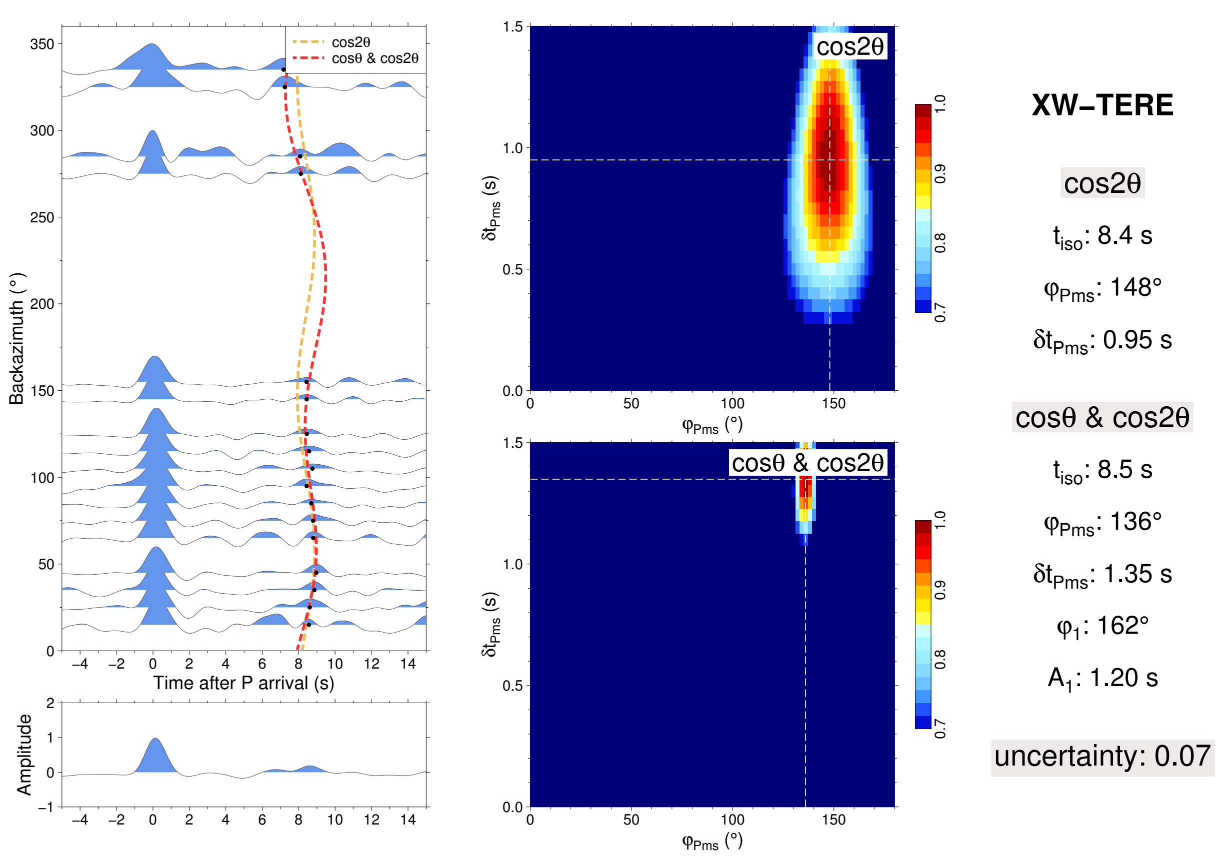

Poor Measurements: Uncertainty larger than 0.4 (4 stations in total)

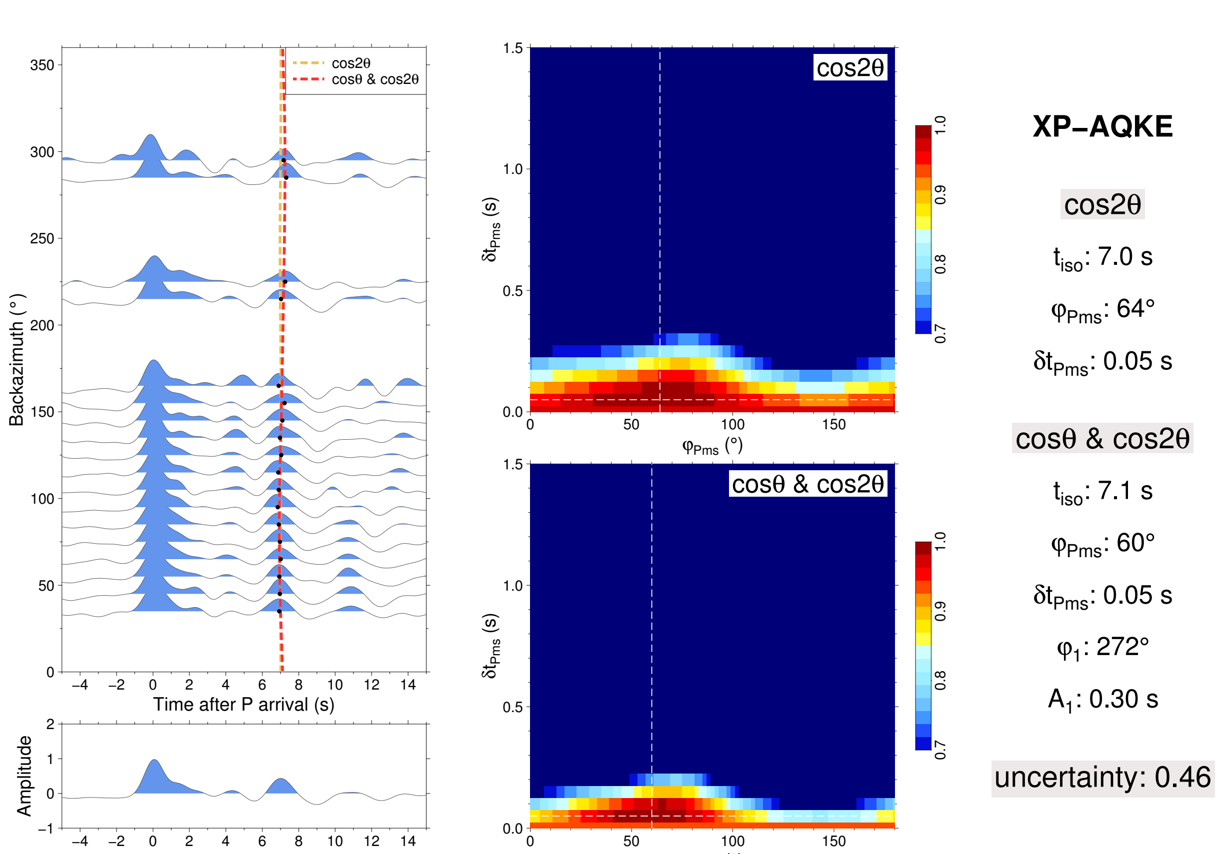

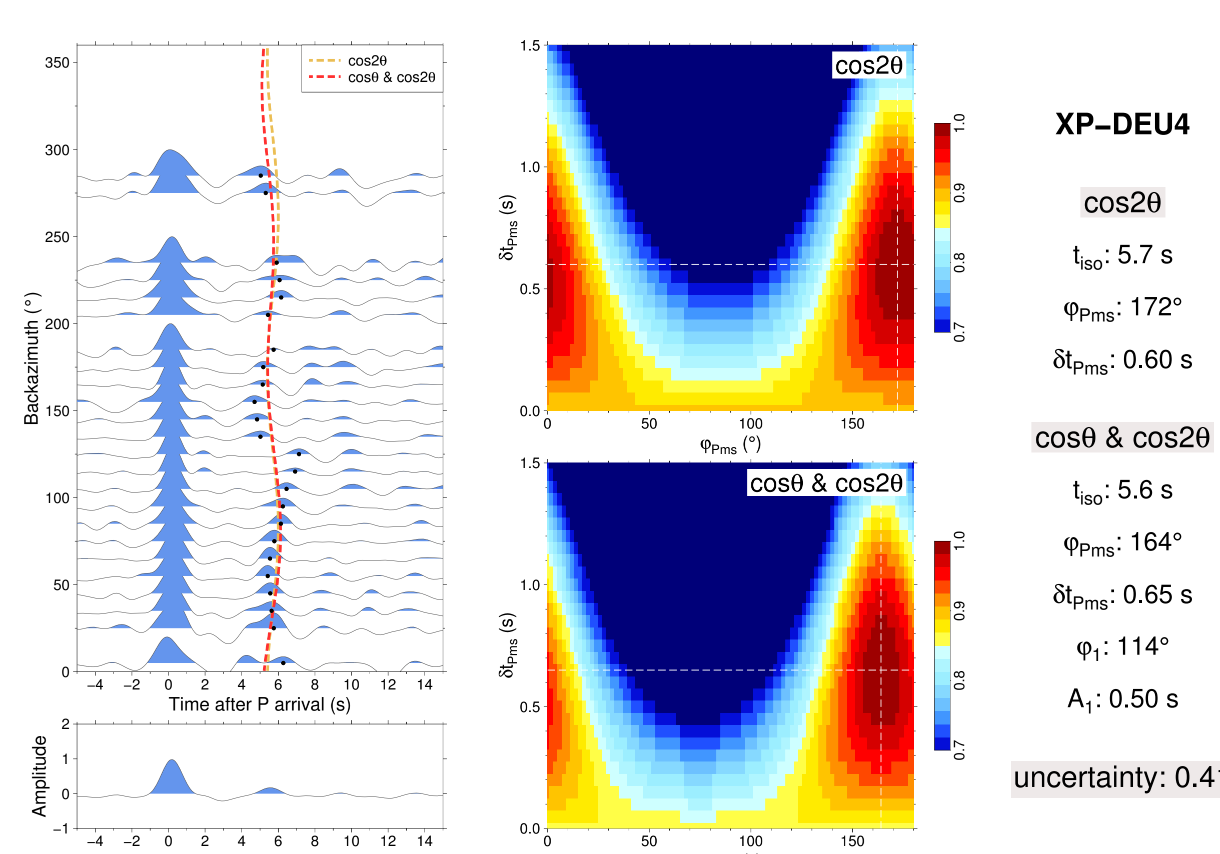

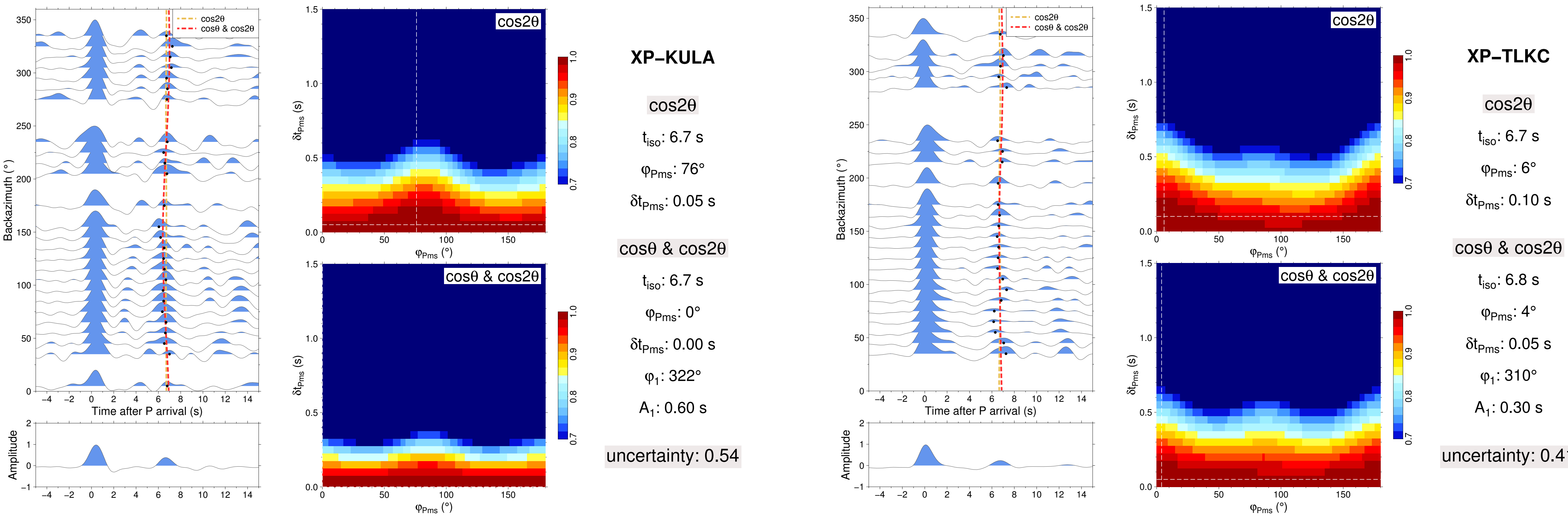

cos2θ
cosθ & cos2θ
Backazimuth (°)
Time after P arrival (s)
Amplitude
δtPms (s)
φPms (°)
XP−KULA
cos2θ
tiso: 6.7 s
φPms: 76°
δtPms: 0.05 s
cosθ & cos2θ
tiso: 6.7 s
φPms: 0°
δtPms: 0.00 s
φ1: 322°
A1: 0.60 s
uncertainty: 0.54
XP−TLKC
cos2θ
tiso: 6.7 s
φPms: 6°
δtPms: 0.10 s
cosθ & cos2θ
tiso: 6.8 s
φPms: 4°
δtPms: 0.05 s
φ1: 310°
A1: 0.30 s
uncertainty: 0.41

Figure S4. Pms moveout fitting measurements at 42 of 55 stations, which are classified into three categories: “Good”, “Poor ($d\_\varphi_{Pms} > 25^\circ$ or $d_{\delta t_{Pms}} > 0.3\ s$)”, and “Poor (Uncertainty > 0.4)”. The other 13 stations suffer from insufficient BAZ coverage (XP-AKMO, XP-FOOD, XP-HORS, XP-KMSK, XP-QUAR, XW-KASH) or indiscernible Pms energy (XP-DEBE, XP-KOKD, XP-KYZY, XP-ORTO, XP-SHOR, XP-TEGL, KN-AAK), and are excluded from the analyses. Left: radial receiver functions plotted as a function of back azimuth and stacked receiver function. Arrival times of the Pms phases and the best-fit harmonic curves are indicated by black dots and dashed lines, respectively. Right: energy maps showing the optimal pair of second-order harmonic parameters (φ_{Pms}-δt_{Pms}). Note that coherent anisotropy parameters (φ_{Pms} and δt_{Pms}) are given by the two harmonic fitting schemes for “Good” measurements, which enhances the credibility of the estimated anisotropy in the presence of a titled Moho.

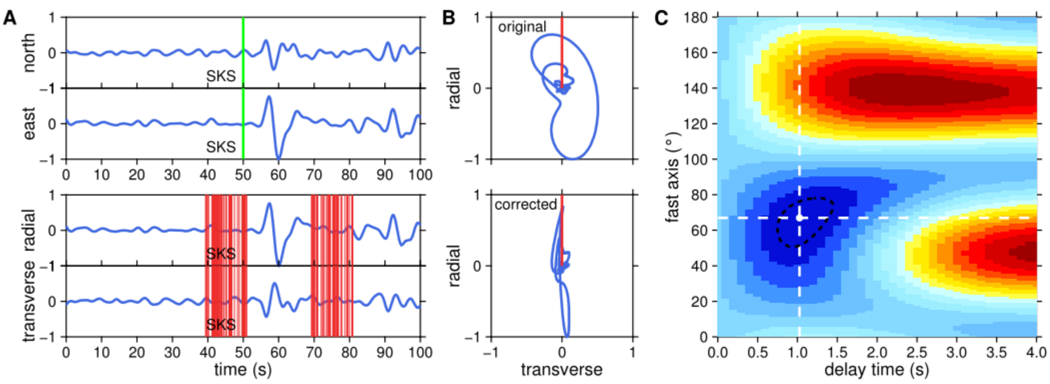

Figure S5. An example of XKS splitting analysis for event 2006-03-07-06:28:55 recorded at station XP-DAMB. (A) Seismogram components in north, east, radial and transverse directions. Green and red solid lines show theoretical phase arrival and 50 different time windows used for the analysis, respectively. (B) Original and corrected particle motion patterns. (C) Energy grid for the corrected transverse component as a function of candidate fast orientations and delay times. The white dot marks the optimal splitting parameters corresponding to the minimum energy. 95% confidence level are indicated by the black dashed contour line.

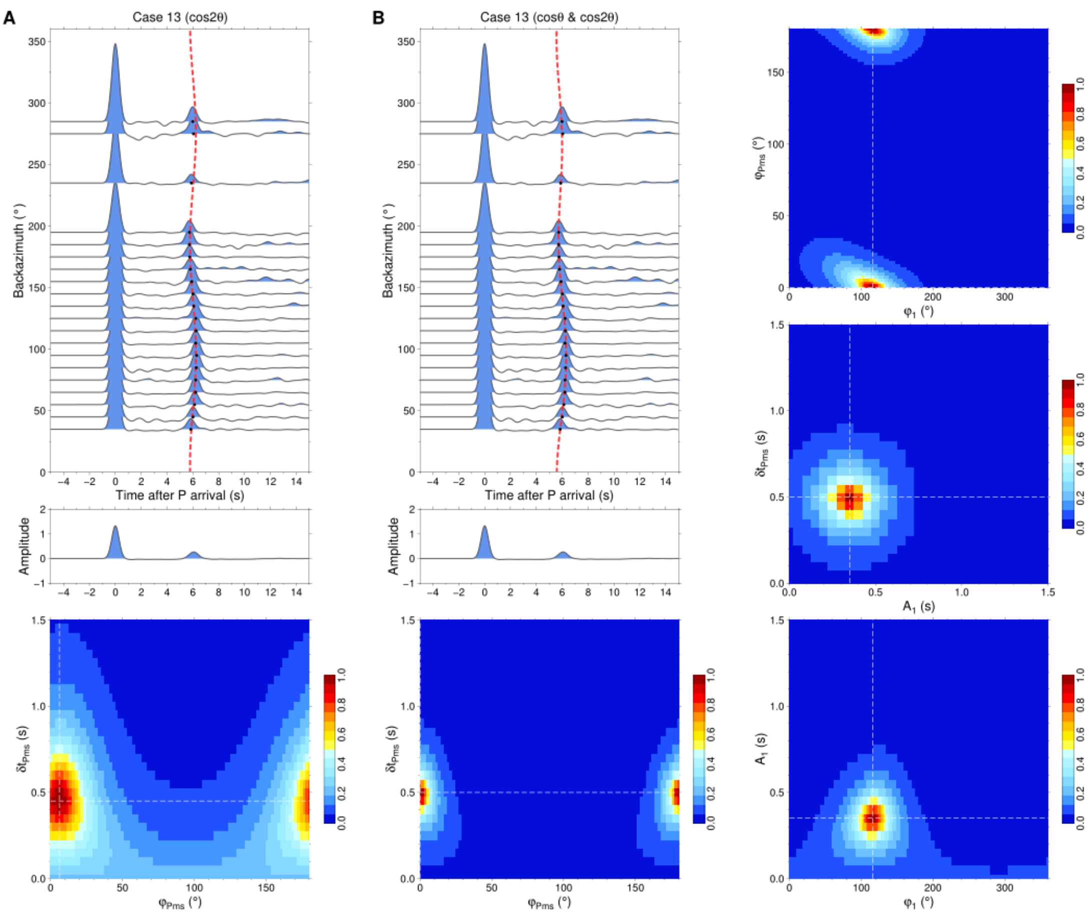

Figure S6. An example of Pms moveout fitting analysis for synthetic case 13 with 4% crustal anisotropy and 10° dipping Moho. The differential angle between the fast symmetry axis and the downdip direction is 45°. The distribution of BAZs and distances is the same as the real data from station XP-KOKD. Random Gaussian noise is also imposed to the synthetic waveforms. (A) The harmonic fitting of Pms arrivals with cos2θ functions. Top: radial receiver functions plotted as a function of back azimuth and stacked receiver function. Arrival times of the Pms phases are indicated by black dots, which show good alignment with the best-fit harmonic curve. Bottom: energy map showing the optimal pair of harmonic parameters (φ_{Pms}-δt_{Pms}). (B) The harmonic fitting of Pms arrivals with cosθ and cos2θ functions. The layout is similar to that of (A), but with three more energy maps (φ_1-φ_{Pms}, A_1-δt_{Pms}, φ_1-A_1) added to the right.

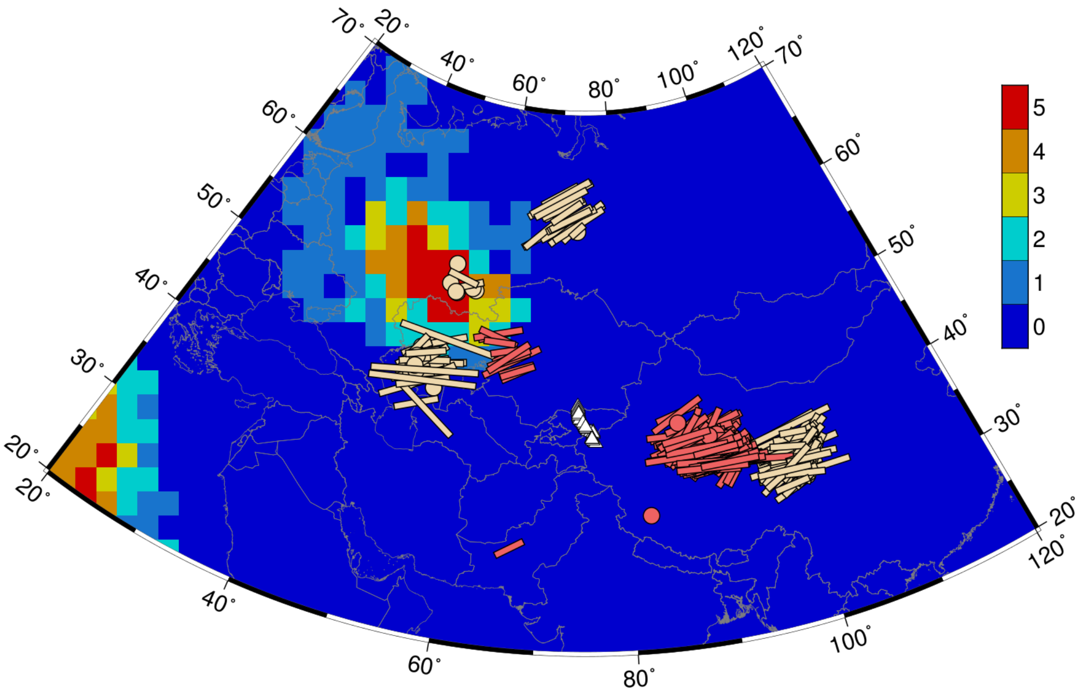

Figure S7. XKS splitting parameters plotted atop the cluster analysis of five global shear wave tomography models at the lower mantle depth (Lekic et al., 2012), zoomed in to the Perm Anomaly region. Background colors indicate the number of tomography models that agree that a given region is anomalously slow. SKS (red) and SKKS (wheat) measurements are shown as bar lines ("good" and "fair") or filled circles ("null"), projected to piercing points at 2700 km depth based on iasp91 Earth model. For non-null measurements, the fast symmetry axis and the amount of splitting are shown by the orientation and length of the bar line, respectively. MANAS Stations are marked as white triangles.

Table S1. Pms moveout fitting measurements at individual stations. Stations are arranged according to their projection point on the orogen-perpendicular profile A-A'.

Block	Station	Lon (°)	Lat (°)	Dist (km)	FD (°)	Delay (s)	Fd_{err} (°)	$Delay_{err}$ (s)
NCTS	XP-CHIC	73.97	43.18	224.5	82	0.65	4	0.08
	KN-EKS2	73.78	42.66	182.3	78	1.20	1	0.09
	XP-IVTA	74.01	42.61	167.7	132	1.10	2	0.07
	KR-FRU1	74.63	42.81	161.3	52	0.30	7	0.08
	XP-SOUR	74.08	42.46	149.7	44	0.95	4	0.16
	KN-AML	73.69	42.13	134.7	0	1.15	2	0.15
	KN-UCH	74.51	42.23	109.8	152	0.70	4	0.11
	XP-BOOB	74.16	42.04	106.0	172	0.50	3	0.02
	XP-MINT	74.22	41.92	91.8	12	0.40	11	0.13
	XP-KYRC	74.33	41.87	82.8	8	0.25	12	0.05
	XW-ARA	74.33	41.85	81.0	122	0.30	15	0.14
	XP-BESM	74.46	41.80	70.8	140	0.55	6	0.07
	KN-KZA	75.25	42.08	64.6	122	0.25	7	0.03
SCTS	XP-KUNT	74.52	41.67	56.3	84	0.50	7	0.15
	XP-TEKE	74.66	41.59	42.1	88	0.70	12	0.10
	XP-KARD	74.87	41.37	12.0	150	0.30	5	0.13
	XP-UCHS	74.98	41.20	-8.3	76	0.65	0	0.00
	XP-ORTK	75.06	41.04	-27.3	142	0.55	4	0.23
	XP-DAMB	75.26	40.89	-50.2	88	0.30	8	0.07
	XP-GOLB	75.28	40.82	-58.2	84	0.60	2	0.09
	XP-KOKA	75.66	40.72	-82.8	64	1.40	3	0.12
	XP-BRID	75.96	40.71	-96.4	86	0.10	4	0.04
	XP-KORU	75.91	40.62	-104.0	108	0.70	3	0.05
	XP-AHQI	75.80	40.07	-151.4	170	0.15	16	0.18
	XP-TRKX	75.78	40.04	-154.1	146	0.50	11	0.11
	XW-TGMT	76.14	40.00	-173.0	78	0.65	2	0.07
	XP-KKTM	76.04	39.87	-181.5	72	0.75	3	0.08

Table S2. List of XKS splitting measurements at individual stations in the categories of "good", "fair" and "null". Stations are arranged according to their projection point on the orogen-perpendicular profile A-A'.

Table S3. Broadband seismic observatories used in the study.

Network	Data Range	Seismometer	Data Acquisition System	Descriptions
Middle AsiaN Active Source project (MANAS, XP) (https://doi.org/10.7914/SN/XP_2005)	2005.07-2007.07	Guralp CMG-3ESP or Strekeisen STS-2	Quanterra Q330	AHQI, AKMO, AQKE, ATSH, BESH, BESM, BOOB, BRID, CHIC, DAMB, DEBE, DEU4, FOOD, GOLB, HORS, IVTA, KAKK, KARD, KKTM, KMSK, KOKA, KOKD, KORU, KRUK, KULA, KUNT, KYRC, KYZY, MINT, MURA, ORTK, ORTO, QUAR, SHOR, SOUR, TEGL, TEKE, TLKC, TRKX, UCHS
Kyrgyz Seismic Telemetry Network (KNET, KN) (https://doi.org/10.7914/SN/KN)	2005.07-2015.06	Strekeisen STS-2	RefTek RT72A-08	AAK, AML, EKS2, KZA, UCH
Kyrgyz Digital Network (KRNET, KR) (https://doi.org/10.7914/SN/KR)	2007.11-2017.06	Guralp CMG-3ESP	Guralp CMG-DM24	ARLS, EKS, FRU, FRU1
Tien Shan Continental Dynamic project (GHENGIS, XW) (https://doi.org/10.7914/SN/XW_1997)	1998.08-2000.08	Guralp CMG-3ESP or Strekeisen STS-2	RefTek RT72A-08	ARA, KAI, KASH, POGR, TERE, TGMT

Table S4. Description of crustal models used in the synthetic tests. In all models, the crust is 50 km thick. The isotropic P and S velocities in the crust are 6.50 and 3.75 km/s, respectively. The P and S velocities in the mantle are 8.04 and 4.50 km/s, respectively.

Model	Description	Aniso.			Moho	
		Trend	Plunge	Strength	Strike	Dip
01	Iso. Flat Moho		Iso.		Flat	
02	Dipping Moho		Iso.		0°	10°
03	Azi. Aniso.	0°	0°	4%	Flat	
04a					0°	
04b	Small Azi. Aniso. Dipping Moho	0°	0°	2%	45°	10°
04c					90°	
05a					0°	
05b	Medium Azi. Aniso. Dipping Moho	0°	0°	4%	45°	10°
05c					90°	
06a					0°	
06b	Large Azi. Aniso. Dipping Moho	0°	0°	8%	45°	10°
06c					90°	

Table S5. Description of back azimuthal distributions and noise levels used in the synthetic tests.

BAZ	Description
01	Full back azimuthal coverage, number of BAZ bands = 36
02	Distribution of station XP-IVTA, number of BAZ bins with data > 24, maximum BAZ gap < 90°
03	Distribution of station XP-KOKD, number of BAZ bins with data > 18, maximum BAZ gap < 120°
04	Distribution of station XP-IVTA, number of BAZ bins with data > 12, maximum BAZ gap < 180°
Noise	**Description**
01	Noise-free
02	Random Gaussian noise added

Table S6. List of all cases in the synthetic tests.

				Cos2θ Only		Cosθ & Cos2θ	
Case	Model	BAZ	Noise	FD (°)	Delay (s)	FD (°)	Delay (s)
01	01	01	01	0	0.00	0	0.00
02	02	01	01	0	0.00	0	0.00
03	03	01	01	0	0.55	0	0.55
04	04a	03	02	0	0.25	-2	0.20
05	04b	03	02	16	0.15	2	0.15
06	04c	03	02	28	0.20	2	0.25
07	05a	01	02	0	0.55	0	0.55
08	05a	02	02	2	0.55	4	0.45
09	05a	03	02	0	0.55	0	0.50
10	05a	04	02	-6	0.60	2	0.50
11	05b	01	02	0	0.55	0	0.55
12	05b	02	02	2	0.50	2	0.45
13	05b	03	02	6	0.45	0	0.50
14	05b	04	02	2	0.55	0	0.50
15	05c	01	02	0	0.55	0	0.55
16	05c	02	02	2	0.50	0	0.50
17	05c	03	02	8	0.45	2	0.50
18	05c	04	02	8	0.70	-6	0.55
19	06a	03	02	0	1.20	0	1.05
20	06b	03	02	2	1.15	6	0.95
21	06c	03	02	0	1.05	-2	1.10